X-ray Detections of Sub-millimetre Galaxies: Active Galactic Nuclei Versus Starburst Contribution

S.P. Johnson[1], G.W. Wilson[1], Q.D. Wang[1], C.C. Williams[1], K.S. Scott[2], M.S. Yun[1], A. Pope[1], J. Lowenthal[3], I. Aretxaga[4], D. Hughes[4], M.J. Kim[5], S. Kim[5], Y. Tamura[6], K. Kohno[6,7], H. Ezawa[8], R. Kawabe[9], T. Oshima[9]

[1] *Department of Astronomy, University of Massachusetts, Amherst, MA 01003, USA*
[2] *North American ALMA Science Center, National Radio Astronomy Observatory, Charlottesville, VA 22903, USA*
[3] *Department of Astronomy, Smith College, Northampton, MA 01063, USA*
[4] *Instituto Nacional de Astrofisica, Optica y Electronica (INAOE), Aptdo. Postal 51 y 216, 72000 Puebla, Pue., Mexico*
[5] *Department of Astronomy & Space Science, Sejong University, Seoul, Korea*
[6] *Institute of Astronomy, University of Tokyo, Osawa, Mitaka, Tokyo 181-0015, Japan*
[7] *Research Center for the Early Universe, University of Tokyo, Hongo, Bunkyo, Tokyo 113-0033, Japan*
[8] *ALMA Project Office, National Astronomical Observatory of Japan, Osawa, Mitaka, Tokyo 181-8588, Japan*
[9] *Nobeyama Radio Observatory, National Astronomical Observatory of Japan, Minamimaki, Minamisaku, Nagano 384-1305, Japan*

6 February 2013

ABSTRACT

We present a large-scale study of the X-ray properties and near-IR-to-radio spectral energy distributions (SEDs) of submillimetre galaxies (SMGs) detected at 1.1mm with the AzTEC instrument across a $\sim$1.2 square degree area of the sky. Combining deep $2-4$ Ms *Chandra* data with *Spitzer* IRAC/MIPS and VLA data within the GOODS-N, GOODS-S and COSMOS fields, we find evidence for AGN activity in $\sim$14 percent of 271 AzTEC SMGs, $\sim$28 percent considering only the two GOODS fields. Through X-ray spectral modeling and multi-wavelength SED fitting using Monte Carlo Markov Chain techniques to Siebenmorgen et al. (2004) (AGN) and Efstathiou, Rowan-Robinson & Siebenmorgen (2000) (starburst) templates, we find that while star formation dominates the IR emission, with star formation rates (SFRs) $\sim 100-1000$ M$_\odot$ yr^{-1}, the X-ray emission for most sources is almost exclusively from obscured AGNs, with column densities in excess of 10^{23} cm^{-2}. Only for $\sim$6 percent of our sources do we find an X-ray-derived SFR consistent with NIR-to-radio SED derived SFRs. Inclusion of the X-ray luminosities as a prior to the NIR-to-radio SED effectively sets the AGN luminosity and SFR, preventing significant contribution from the AGN template. Our SED modeling further shows that the AGN and starburst templates typically lack the required 1.1 mm emission necessary to match observations, arguing for an extended, cool dust component. The cross correlation function between the full samples of X-ray sources and SMGs in these fields does not indicate a strong correlation between the two populations at large scales, suggesting that SMGs and AGNs do not necessarily trace the same underlying large scale structure. Combined with the remaining X-ray-dim SMGs, this suggests that sub-mm bright sources may evolve along multiple tracks, with X-ray-detected SMGs representing transitionary objects between periods of high star formation and AGN activity while X-ray-faint SMGs represent a brief starburst phase of more normal galaxies.

Key words: galaxies: active – galaxies: starburst – galaxies: high-redshift – submillimetre: galaxies – X-ray: galaxies

1 INTRODUCTION

Large blank-field surveys made at (sub-)millimetre wavelengths have identified a large population of bright, high-redshift galaxies (e.g. Hughes et al. 1998; Coppin et al. 2006; Bertoldi et al. 2007; Perera et al. 2008; Weiβ et al. 2009; Scott et al. 2010, and references therein). These sub-millimetre galaxies (SMGs) are characterized by high infrared (IR) luminosities, $\gtrsim 10^{12}$ L$_\odot$ (Blain et al. 2004; Chapman et al. 2005), and a redshift distribution peaking around $z \sim 2$ (Chapman et al. 2005). SMGs are therefore believed to be the high-redshift analogs to local ultra-luminous IR galaxies (ULIRGs) and are possible progen-

itors of today's massive ellipticals (e.g. Smail et al. 2004; Chapman et al. 2005). However, SMGs at $z \sim 2$ are more numerous than local ULIRGS by several orders of magnitude and likely dominate the total IR luminosity density at $z \sim 2$ (Le Floc'h et al. 2005; Pérez-González et al. 2005; Hopkins et al. 2010). The origin of these luminous, high-redshift sources is still under debate due, in part, to the low angular resolution at (sub-)millimetre wavelengths of current instruments and the relative faintness of likely counterparts. Multi-wavelength and IR spectroscopic follow-up studies of SMGs using *Spitzer* (see, for example, Menéndez-Delmestre et al. 2007; Pope et al. 2008; Nardini et al. 2008) suggest that SMGs are largely dust-obscured starburst systems with star formation rates (SFRs) ~ 1000 M$_\odot$ yr^{-1}. However, it is becoming increasingly apparent through the high X-ray detection rate of SMGs ($\sim 30-50\%$, see Alexander et al. 2005a,b; Laird et al. 2010; Georgantopoulos, Rovilos & Comastri 2011) and SMG case studies (i.e., Tamura et al. 2010) that emission from active galactic nuclei (AGNs) may also be a crucial component to the energetic output of SMGs.

The likely connection between starburst and AGN activity in SMGs is further supported by the concurrent nature of the cosmic SFR and black hole accretion with peaks at $z \sim 2$ (e.g., Le Floc'h et al. 2005; Merloni 2004). Simulations of SMG formation in a merger-driven scenario also suggest that the SMG phase precedes rapid growth of a central AGN (Narayanan et al. 2010). SMGs may therefore represent an important phase in galaxy evolution and may shed light on the origin of observed relations between AGN activity and stellar mass in local galaxies (i.e. the M-σ relation; Ferrarese & Merritt 2000; Gebhardt et al. 2009; Gultekin et al. 2009). One should be cautious, however, in extrapolating the starburst-AGN connection to the most extreme objects (i.e. radio-loud AGN, Dicken et al. 2012, and references therein) though such cases are a fundamentally different population of sources. Unfortunately, while there are a multitude of methods for studying AGN and star formation, disentangling their relative contributions to a galaxy's bolometric output remains challenging. Obtaining redshifts and other information via optical/ultra-violet imaging and spectroscopy is exceptionally difficult as SMGs are both distant and optically thick (see review by Blain et al. 2002). IR spectroscopy of SMGs typically show strong polycyclic aromatic hydrocarbon (PAH) features associated with star-forming regions, although there are cases of power-law-like spectra indicative of AGN (Menéndez-Delmestre et al. 2007; Coppin et al. 2008; Nardini et al. 2008; Pope et al. 2008). Arguably, the best indicator for AGN activity is hard X-rays (>2 keV), which penetrate obscuring dust up to the Compton thick limit (neutral hydrogen column densities of N$_H \gtrsim 10^{24}$ cm^{-2}). X-ray detections are not uniquely attributable to AGN, however, as high SFRs may produce numerous high-mass X-ray binaries (HMXBs) that mimic the emission of low-luminosity AGNs.

In the past decade there have been few studies that consider X-ray counterparts to SMGs for evidence of AGN activity, though this number has expanded in recent years. Alexander et al. (2005a,b) (hereafter A05a,b) provide the earliest analysis by examining the *Chandra* counterparts to SCUBA (Holland et al. 1999) 850μm identified sources

in the Great Observatories Origins Deep Survey (GOODS) North field. In their sample of 20 SMGs with radio and spectroscopic redshift identifications taken from Chapman et al. (2005), they find that ~ 75 percent have X-ray properties consistent with obscured (N$_H \gtrsim 10^{23}$ cm^{-2}) AGN activity. Accounting for SMGs without spectroscopic redshifts, they suggest that the true X-ray detection rate may be significantly lower, $\gtrsim 28$ percent. However, the A05a,b sample may contain biases introduced through the Chapman et al. (2005) SCUBA source catalog, which consists of observations of known radio sources and low signal-to-noise (S/N$<3.5\sigma$) sources and thus may not be representative of the entire bright SMG population (see also, Younger et al. 2007). Further X-ray/SMG counterpart analysis has been provided by Laird et al. (2010) (hereafter LNPS10), who find a ~ 45 percent X-ray detection rate to radio and/or *Spitzer*-identified SCUBA sources (Pope et al. 2006) with a ~ 20-29 percent AGN identification rate based on X-ray spectral modeling. LNPS10 find that the bolometric FIR emission is dominated by star formation in the majority of their sources (~ 85 percent) after including available *Spitzer* photometry; consistent with A05a,b and other IR studies of SMGs (i.e. Menéndez-Delmestre et al. 2007; Valiante et al. 2007; Menéndez-Delmestre et al. 2009).

More recently, the studies of Georgantopoulos, Rovilos & Comastri (2011) (hereafter GRC11), Hill & Shanks (2011) and Bielby et al. (2012) have utilized LABOCA data in the Extended *Chandra* Deep Field South (ECDFS, Weiβ et al. 2009) and William Herschel Deep Field. The analysis of GRC11 is similar to that of LNPS10 who also find an AGN fraction of $< 26 \pm 9$ percent with the mid-IR emission dominated by starburst activity, though the fraction of starburst-powered X-ray sources is lower than estimated by LNPS10. The works of Hill & Shanks (2011) and Bielby et al. (2012) consider a more statistical approach, utilizing the full catalogs rather than individual sources as in A05a,b, LNPS10 and GRC11, though find a similar SMG/X-ray detection rate (~ 20 percent). They also find that obscured AGNs preferentially have greater sub-mm emission than unobscured AGNs; a result confirmed through ELVA observations by Heywood et al. (2012). Lutz et al. (2010) find a similar relation in the ECDFS where the X-ray luminosity and absorbing column density for bright AGNs, $L_{2-10\text{keV}} \gtrsim 10^{43}$ ergs s^{-1}, is correlated with the 870μm flux, implying a close connection to star formation. This assumes, however, that the X-ray emission is purely from the AGN while the 870μm flux is only from star formation. Furthermore, the Lutz et al. (2010) study does not account for X-ray-bright SMGs, which may potentially bias the stacking results.

To recap, X-ray studies to-date find that the AGN fraction of SMGs is in the range of ~ 20-45 percent and that the bolometric IR luminosity of SMGs is dominated by starbursts.

In this work, we examine the identification rate and contribution of AGNs to the emission at various wavelength regimes in AzTEC SMGs. Our sample consists of *Chandra* X-ray counterparts to AzTEC 1.1 mm sources found in the GOODS-North, GOODS-South and COSMOS fields, providing a total *Chandra* sky coverage of ~ 1.15 square degrees (~ 0.12, ~ 0.11 and ~ 0.92 square degrees, respectively) with

more than 2600 identified X-ray sources. This large sample size will reduce any biases due to cosmic variance in previous studies. Furthermore, we do not base our sample selection and counterpart identification on prior source association, thus removing any possible pre-identification bias. The available multi-wavelength photometry in these fields, including *Spitzer* IRAC and MIPS, will provide additional constraints on the AGN identification rate and contribution to the bolometric output of our sources.

We begin with a description of the AzTEC and *Chandra* data and reduction procedures. We then detail our method for identifying X-ray counterparts to the AzTEC sources and subsequent multi-wavelength counterparts. Our analysis of the X-ray-identified AzTEC sources follows a two-pronged approach: (1) applying X-ray spectral models and SED templates to the X-ray spectra and near-IR-to-radio SED, which will provide the basic information concerning the contribution of AGN and star formation in each wavelength regime; and (2) linking the X-ray spectral fits to the near-IR-to-radio SED modeling, thus providing greater insight into the AGN/star formation connection. Our SED fitting differs from typical SED analyses (e.g. Serjeant et al. 2010) in that we employ a Monte Carlo Markov Chain (MCMC) technique. We close by comparing the implications of our work to those of previous X-ray/SMG results in addition to the X-ray/SMG cross-correlation relation. Additional analysis of our data, including source stacking and IR-optical-UV fitting, will be presented in future publications.

Throughout this work, we assume a flat ΛCDM cosmology with $H_0 = 70$ km s^{-1} Mpc^{-1}, $\Lambda_0 = 0.73$ and $\Omega_M = 0.27$.

2 OBSERVATIONS AND DATA PROCESSING

2.1 AzTEC: 1.1 mm Observations

AzTEC (Wilson et al. 2008) is a 144-element bolometer array operating at 1.1mm and installed on the 50m Large Millimetre Telescope (LMT; Schloerb 2008). Prior to its installation on the LMT, AzTEC has performed several science observations on the James Clerk Maxwell Telescope (JCMT) and the Atacama Sub-millimetre Telescope Experiment (ASTE), including blank fields (namely GOODS-N, GOODS-S and COSMOS) and high redshift radio clusters. Here, we briefly describe the AzTEC observations and 1.1 mm source sample that will be used in our analysis.

During the JCMT 2005-2006 observing campaign, Perera et al. (2008) imaged a $21' \times 15'$ area of the GOODS-N region. During the 2007 and 2008 observation seasons on ASTE, AzTEC imaged both GOODS-S (Scott et al. 2010) and the one square degree area of COSMOS (Aretxaga et al. 2011). In reducing the raw time-steams for each set of observations, an iterative technique using Principle Component Analysis (PCA) is used to filter out the atmospheric signal that dominates the raw observed data. Downes et al. (2011) provides a discussion on correcting the PCA transfer function and lists revised catalogs for previously released AzTEC data. Here, we use the revised catalogs of Downes et al. for GOODS-N and GOODS-S; the COSMOS catalog of Aretxaga et al. (2011) follows this prescription. The final AzTEC maps are constructed to have uniform coverage and sensitivity, providing a 1σ rms of $\sim$1.3 mJy in GOODS-N

and COSMOS. The GOODS-S map reaches the confusion limit of AzTEC on ASTE for a depth of $(1\sigma) \sim$0.6 mJy rms. Sources are defined as peaks in the signal map with S/N$\geqslant$3.5σ, resulting in a total sample of 277 AzTEC sources (40, 48 and 189 in GOODS-N, GOODS-S and COSMOS, respectively) where $\lesssim$20 are expected to be false detections. Note, however, that the false detection rate is estimated for a S/N threshold of $\sim$3.5σ and decreases rapidly for higher source S/N. For the following analysis, we use the full sample of 277 AzTEC sources, applying no additional source-selection criteria.

2.2 *Chandra* Observations

The *Chandra* X-ray Observatory provides deep observations of the GOODS-N, GOODS-S and COSMOS fields (for details on the observations see Alexander et al. 2003; Luo et al. 2008; Elvis et al. 2009, respectively) with total exposure times of $\sim$2Ms in each field. More recently, an additional $\sim$2Ms has been added to GOODS-S with 31 additional pointings; bringing the final integrated exposure time to $\sim$4Ms (Xue et al. 2011). Due to the pointing strategy for COSMOS, effective exposures only reach $\sim$200ks for the inner $\sim$0.5 sq. degree (see also Elvis et al. 2009). As a result, the X-ray photon statistics in COSMOS are very poor, leading to weak constraints on the X-ray spectral properties (§ 3.1). This is somewhat offset by its larger area than the GOODS fields by allowing for more potential counterparts (§ 2.3). On the other hand, the deep 4Ms data in GOODS-S provides the greatest improvement to the counting statistics, and thus spectral modeling, to date; a valuable asset for potentially faint and highly obscured AGNs. All of the fields were imaged with the Advanced CCD Imaging Spectrometer Imaging array (ACIS-I), which is composed of four CCDs arranged in a 2×2 grid that operate together to provide a $\sim 17' \times 17'$ field-of-view with sub-arcsecond resolution at the telescope aim-point, degrading with increasing off-axis distance.

To ensure uniformity in our analysis, all observations were re-reduced using *Chandra* Interactive Analysis of Observations (CIAO version 3.4) routines and custom routines developed for working with merged X-ray data sets; using the published X-ray catalogs of Alexander et al. (2003), Luo et al. (2008), Xue et al. (2011) and Elvis et al. (2009) would have required additional calibrations for compatibility. Event files and exposure maps constructed in the 0.5-8.0 keV energy range were made for all observations and then merged to produce final maps for the three fields.

We use the source detection method of Wang (2004), with a false detection probability threshold of 10^{-6}, to produce X-ray source lists from the final images for cross-correlation with the AzTEC sample and spectral extraction. This detection method uses a wavelet analysis of the input images (in this case, the final merged X-ray images for each field) followed by a sliding-box map detection and maximum likelihood analysis for both source centroiding and optimal photometry. During the source detection, the X-ray maps are divided into different energy bands (i.e. 0.5-8.0 keV full band, 0.5-2.0 keV soft band and 2.0-8.0 keV hard band), resulting in a source catalog that includes all sources found in each energy band along with their respective count rates and positional uncertainties. The source detection process

also produces a list of source regions, which are defined as circular regions with radius equal to twice the 90 percent energy encircled fraction (defined according to the PSF at the source position).

COSMOS poses a dilemma for source detection due to the blending of PSFs from the tiling of observations. To avoid this issue, we perform the X-ray source detection on the individual observations and then combine the resulting source lists into a final catalog. Derived parameters are recalculated for each source using the final COSMOS map, with extraction radii determined from the smallest PSF corresponding to each source. Alternatively, one could simply average the sub-catalogs to produce the final catalog; however, this may exclude X-ray counts present in an image where the source was not initially detected. Certainly, this method has difficulty in detecting the faintest sources present in COSMOS; nevertheless, this will not significantly influence our results given the already low depth of COSMOS compared to the two GOODS fields.

Combining the source lists from each field results in a total of 2630 X-ray sources available for our study. Individually, there are 478, 526, and 1626 sources in GOODS-N, GOODS-S, and COSMOS, respectively. Despite the differences in data reduction and source detection, our source lists recover $\gtrsim$90 percent of those from the published catalogs of Alexander et al. (2003), Luo et al. (2008), Xue et al. (2011) and Elvis et al. (2009). However, we miss many faint sources from the published catalogs due to our more stringent false detection threshold of 10^{-6} versus $\sim$1-2$\times10^{-5}$ for the other catalogs.

2.3 Counterpart Candidates

2.3.1 Chandra Counterparts

The beam size of AzTEC on the JCMT and ASTE is 18$''$ and 28$''$ FWHM, respectively, making reliable X-ray counterpart identification challenging. Following the method of Chapin et al. (2009), we use a fixed search radius of 6$''$ in GOODS-N and 10$''$ in GOODS-S and COSMOS to find potential counterparts to the AzTEC sources. Our choice of 10$''$ in GOODS-S and COSMOS is consistent with a derived search radius for a source with S/N$\sim$5.5 on the ASTE telescope according to Ivison et al. (2007) and roughly corresponds to the average search radius for the AzTEC GOODS-S catalog (Scott et al. 2010). Simulations in each field agree well with the Ivison et al. (2007) estimate and show that sources with S/N$\gtrsim$3.5 are recovered within the respective search radii >85 percent of the time. Extending the search radius beyond our adopted value increases the number of X-ray counterparts; however, these additional X-ray sources are unlikely to be true counterparts (see below).

As shown in Figure 1, there is significant overlap between the AzTEC and *Chandra* maps. Considering only the overlapping regions, our sample is limited to 271 (39, 47, and 185 in GOODS-N, GOODS-S, and COSMOS, respectively) of the initial 277 AzTEC sources and 2229 (397, 429, 1403 respectively) of the 2630 *Chandra* sources. Of the remaining 271 AzTEC sources, we find 38 with at least one X-ray counterpart (8, 16, and 14 for GOODS-N, GOODS-S, and COSMOS, respectively); 5 have 2 potential counterparts and 1 has 3. For those sources with multiple potential *Chandra*
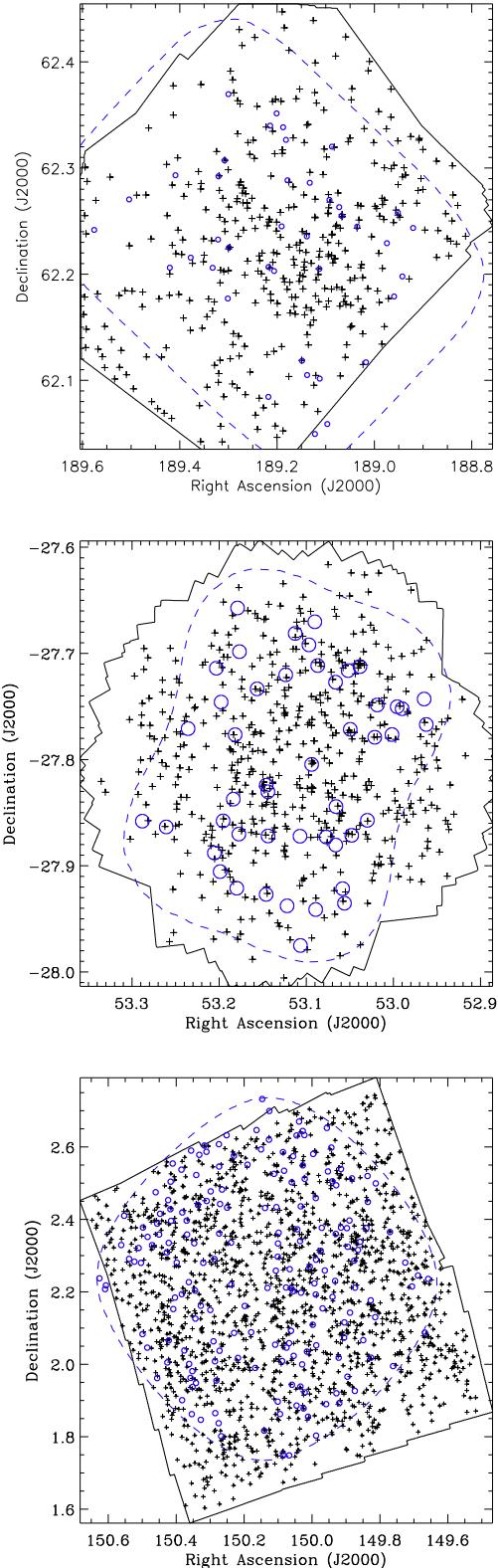

Figure 1. *Chandra* (solid black line) and AzTEC (dashed blue line) coverage regions for GOODS-N (upper), GOODS-S (middle) and COSMOS (lower). The AzTEC coverage given here corresponds to the 50 percent uniform coverage region used for source detection. Small circles with radii equal to the AzTEC beamsize (18$''$ in GOODS-N and 28$''$ in GOODS-S and COSMOS) are plotted at the AzTEC source positions. X-ray source positions are indicated by the small 'plus' symbols.

counterparts, we treat each source individually and do not attempt to split the AzTEC flux as we have no prior information on how it may be related to the potential X-ray sources. Overlapping spectral regions for these sources is not an issue as the uncertainty in the X-ray spectra is dominated by the low counting statistics. There are a total of 45 X-ray sources associated with the AzTEC sample, of which only 2-3 are expected to be false identifications due to random alignments. Comparatively, the expected number of X-ray pairs for the entire sample of 271 AzTEC sources, assuming a purely random X-ray source population, is ∼14. The AzTEC/X-ray identification rate is therefore ∼14 percent, lower than estimates reported by A05a and LNPS10 due to the shallower X-ray depth of the COSMOS field; removing it increases the identification rate to ∼28 percent.

To assess the robustness of our X-ray counterpart identifications, we compute the probability P of random association for a given AzTEC/X-ray pair given the search radii and X-ray source densities (2.97, 3.14 and 1.39×10^{-4} arcsec^{-2} for GOODS-N, GOODS-S and COSMOS, respectively) using the method of Downes et al. (1986), which corrects for the use of a finite search radius and flux-limited source density. The majority of the AzTEC/X-ray pairs (32/45) have P≤0.05 which we define as a 'robust' counterpart, the remaining AzTEC/X-ray pairs, with P=0.05-0.10, are 'tentative' associations. Table 1 provides the list of the *Chandra*-detected AzTEC sources along with their relevant source properties and P values.

Through this counterpart analysis, we are implicitly assuming that the AzTEC and X-ray source populations are physically associated and that the two populations are not significantly clustered. If, on the other hand, the X-ray and SMG source populations are clustered, then we are more likely to falsely associate sources and misinterpret the relation between AGN and starburst systems. Almaini et al. (2003) found evidence for correlation between *Chandra* and SCUBA 850μm source populations in the European Large Area ISO Survey (ELAIS) N2 field at the 4.3σ significance level and thus concluded that while they trace the same large scale structure, the AGN and starburst phases are not necessarily co-existent. Based on our cross-correlation analysis (see § 4.2), we find no evidence for significant correlation between deep *Chandra* and AzTEC source populations in general.

2.3.2 Multi-wavelength Counterparts

Thanks to the extensive multi-wavelength coverage in the GOODS and COSMOS fields, we are able to supplement the millimetre and X-ray data of our AzTEC sample with additional photometry and spectroscopic/photometric redshifts from the GOODS and COSMOS public data sets. Accurate redshifts are the most crucial given the broad redshift distribution of SMGs and the sensitivity of X-ray spectral modeling to redshift (§ 3.1). Across the three fields, we utilize publicly available VLA (1.4 GHz; Miller et al. 2008; Kellermann et al. 2008; Morrison et al. 2010), *Spitzer* IRAC (3.6, 4.5, 5.8, 8.0 μm) and MIPS

(24 μm) SIMPLE[1], GOODS[2], and FIDEL[3] data, including spectroscopic/photometric redshift catalogs where available (e.g. Barger et al. 2003; Barger, Cowie & Wang 2008; Santini et al. 2009; Silverman et al. 2010). Multi-wavelength counterparts and redshifts for COSMOS were obtained by cross-referencing our detected sources with Elvis et al. (2009) and the COSMOS team's web-based data repository.[4] In cross-referencing our AzTEC/X-ray sources with other catalogs, we use a search radius of 2″, the average X-ray positional uncertainty, centered on the X-ray counterparts. For each potential AzTEC/X-ray pair, we find no more than one potential counterpart in the VLA and *Spitzer* catalogs; these sources have been cross-checked with other AzTEC counterpart publications (i.e. Chapin et al. 2009; Yun et al. 2012) and show excellent agreement. For reference, ≲ 1 VLA/*Spitzer* source is expected to be a misassociation due to random alignments over all three fields. For cases where we have IRAC but no MIPS identifications, we estimate a 5σ MIPS flux upper limit through the photometric error of the MIPS source nearest to the IRAC position. A complete catalog of the multi-wavelength photometry and redshift data for our sample is given in Table 2.

3 ANALYSIS

With our sample of X-ray selected AzTEC sources in hand, we now examine their physical properties through a variety of methods. We start with modeling of the X-ray spectra.

3.1 X-ray Spectral Modeling

X-ray sources with $L_{2.0-10.0\text{keV}} \gtrsim 10^{42}$ ergs s^{-1} are generally believed to be powered almost exclusively by AGN with absorption due to modest amounts of dust and gas within the host galaxy. A05b showed that X-ray-identified SMGs are predominantly heavily obscured, possibly even to the Compton thick limit with column densities of $N_{\text{H}} \geqslant 10^{23}$ cm^{-2}. For the most extreme cases of obscuration, a buried AGN may only be visible in light scattered off of the obscuring torus. Alternatively, if SMGs are powered by a high rate of star formation, then the observed X-ray emission could result from the stellar population, powered by numerous high-mass X-ray binaries (HMXB). For comparison, a typical SMG with SFR in the range of 100-1000 M$_\odot$ yr^{-1} would produce an X-ray source with 2.0-10.0 keV luminosity of $\sim 10^{41-42}$ ergs s^{-1} (Persic et al. 2004, hereafter P04).

For our sample of AzTEC/X-ray sources, we first extract their source and local background spectrum in the 0.5-8.0 keV observed energy range using the region files defined from our source detection (see § 2.2). Note that background spectra are taken from source-removed event files to avoid contamination from nearby sources. The spectra are fitted in the XSPEC (version 12.4.0, Arnaud 1996, 2003) software package using the C-statistic (Cash 1979) due to the low photon counts in many of the spectra (see Table 1). In order to improve the counting statistics within each bin, we

---

[1] http://www.astro.yale.edu/dokkum/simple/
[2] http://www.stsci.edu/science/goods/
[3] http://ssc.spitzer.caltech.edu/legacy/abs/dickinson2.html
[4] http://irsa.ipac.caltech.edu/Missions/cosmos.html

Table 1. *Chandra* identifications of AzTEC sources in GOODS-N, GOODS-S and COSMOS. Errors are given at the 1σ confidence level. Col.(1): AzTEC source ID prefixed by field (i.e. AzGN24 for source 24 in the AzTEC GOODS-N catalog). Col.(2): *Chandra* ID following IAU standards. Col.(3): Positional offset between AzTEC and *Chandra* sources. Errors are derived from *Chandra* positional uncertainty. Col.(4): *Chandra* 0.5-8.0 keV full band count rate. Cols.(5): Total counts within the source regions as defined from our X-ray source detection. Col.(6): Estimated background counts within the source regions. Col.(7): deboosted AzTEC source flux (see section 3.5 of Austermann et al. 2010 and section 6.2 of Scott et al. 2010). Col.(8): Probability P of the *Chandra* source being a random association.

SMM ID	*Chandra* Coordinate (J2000)	δ_x ('')	0.5-8.0 keV count rate (cnts ks^{-1})	Source Counts	Background Counts	1.1mm Flux (mJy)	P
(1)	(2)	(3)	(4)	(5)	(6)		
AzGN24	J123608.57+621435.8†	5.4±0.8	0.031±0.007	98	61	3.1±1.3	0.03
AzGN16a	J123615.83+621515.9†	3.1±0.5	0.067±0.008	223	42	3.6±1.3	0.03
AzGN16b	J123615.93+621522.0	4.6±0.9	0.013±0.005	51	49	3.6±1.3	0.02
AzGN16c	J123616.08+621514.1†	3.7±0.4	0.089±0.009	184	46	3.6±1.3	0.02
AzGN10	J123627.52+621218.3	2.7±0.5	0.043±0.007	95	42	4.5±1.3	0.02
AzGN11	J123635.86+620707.8	1.8±2.7	0.176±0.017	812	565	4.1±1.3	0.01
AzGN14	J123651.70+621221.7	4.4±0.4	0.222±0.015	301	42	3.7±1.3	0.03
AzGN7a	J123711.32+621331.1†	3.3±1.0	0.047±0.008	173	106	5.3±1.3	0.02
AzGN7b	J123711.98+621325.8†	4.5±1.1	0.043±0.008	150	100	5.3±1.3	0.03
AzGN26	J123713.84+621826.2†	0.5±1.5	0.195±0.016	486	262	2.8±1.4	0.001
AzGN23	J123716.63+621733.4	2.3±1.3	2.101±0.045	2789	218	3.1±1.3	0.01
AzGS29	J033158.25-274458.8	9.6±2.9	0.079±0.013	1865	1542	2.3±0.6	0.09
AzGS8a	J033204.48-274643.3	8.7±1.5	0.201±0.012	1111	650	3.4±0.6	0.09
AzGS8b	J033205.34-274644.0	2.8±1.4	0.150±0.010	917	591	3.4±0.6	0.03
AzGS10	J033207.12-275128.6	2.9±2.2	0.020±0.008	715	703	3.8±0.7	0.03
AzGS38a	J033209.26-274240.9	3.7±2.7	0.078±0.011	1923	1206	1.7±0.6	0.04
AzGS38b	J033209.71-274249.0	8.0±2.2	0.138±0.013	1705	1106	1.7±0.6	0.09
AzGS1	J033211.39-275213.7	3.2±1.4	0.774±0.021	2338	609	6.7±0.6	0.03
AzGS13	J033212.23-274620.9	5.7±0.8	0.247±0.012	789	260	3.1±0.6	0.07
AzGS7	J033213.88-275600.2	8.7±3.4	0.189±0.019	1932	1497	3.8±0.6	0.09
AzGS11	J033215.32-275037.6	6.6±0.8	0.065±0.007	378	236	3.3±0.6	0.08
AzGS17a	J033222.17-274811.6	6.6±0.3	0.059±0.006	176	52	2.9±0.6	0.08
AzGS17b	J033222.56-274815.0	1.6±0.5	0.029±0.004	123	53	2.9±0.6	0.01
AzGS34	J033229.46-274322.0	9.8±1.4	0.027±0.006	492	392	1.7±0.6	0.09
AzGS20	J033234.78-275534.0	4.8±2.6	0.108±0.013	1853	1490	2.7±0.6	0.05
AzGS14	J033235.18-275215.7	9.2±1.0	0.034±0.006	381	295	2.9±0.6	0.09
AzGS16	J033238.01-274401.2	6.3±1.6	0.012±0.006	392	344	2.7±0.6	0.07
AzGS18	J033244.02-274635.9	5.7±0.6	0.188±0.011	592	198	3.1±0.6	0.07
AzGS25	J033246.83-275120.9	6.9±1.3	0.041±0.007	521	400	1.9±0.6	0.08
AzGS9	J033302.94-275146.9	5.1±3.1	0.204±0.020	1421	1097	3.6±0.6	0.06
AzC56	J095905.05+022156.4	2.7±2.6	0.087±0.040	9	3	4.7±1.1	0.01
AzC181	J095929.70+021706.4	7.8±1.8	0.079±0.029	24	9	2.9±1.2	0.04
AzC101	J095945.15+023021.1	6.9±3.4	0.284±0.065	56	29	3.8±1.1	0.04
AzC71	J095953.85+021853.6	5.8±0.9	0.202±0.048	32	9	4.3±1.1	0.03
AzC118	J095959.96+020633.1	7.0±2.3	0.113±0.033	23	6	3.7±1.2	0.02
AzC43	J100003.73+020206.4	2.3±2.8	0.125±0.047	77	59	4.8±1.1	0.009
AzC81	J100006.11+015239.2	3.1±1.0	0.192±0.041	48	9	4.1±1.1	0.01
AzC45	J100006.55+023259.3	2.2±1.4	0.211±0.051	32	4	4.8±1.1	0.009
AzC44a	J100033.61+014902.0	3.2±0.9	0.303±0.054	55	5	5.0±1.2	0.01
AzC44b	J100033.75+014906.3	6.3±4.5	1.137±0.121	78	40	5.0±1.2	0.03
AzC17	J100055.34+023441.1	8.6±2.1	4.970±0.323	317	31	6.2±1.1	0.04
AzC147	J100107.46+015718.1	2.1±3.2	0.296±0.062	82	42	3.2±1.2	0.007
AzC108	J100116.15+023606.9	7.5±3.8	3.090±0.610	45	12	4.0±1.2	0.04
AzC85	J100139.73+022548.5	9.0±0.8	0.333±0.085	37	3	4.0±1.1	0.04
AzC11	J100141.02+020404.8	8.7±1.8	0.179±0.064	12	4	7.9±1.1	0.04

† Source also detected in LNPS10.

have re-binned the spectra to fixed width spectral channels of ∼43.8 eV.

In fitting the X-ray spectra, we consider two different classes of spectral models: (1) an intrinsically absorbed power-law, indicative of AGN; and (2) a stellar model based on HMXB emission including intrinsic absorption. These models are designed to be simple, yet physically meaningful, representations of the X-ray emission. For comparison with previous works, we also consider a simple power-law with only Galactic absorption, represented by the XSPEC model PHA(PO), to measure the effective photon index Γ_{Eff}. As the C-statistic itself is not a measure of the "goodness-of-fit" (see, however, Lucy 2000), we use the XSPEC GOODNESS command for comparing the different spectral models (§ 3.1.3).

Table 2. VLA, *Spitzer* IRAC/MIPS and redshift information for the X-ray identified AzTEC sources. Spectroscopic and photometric redshift information for the AzTEC/X-ray sources was taken, primarily, from publicly available redshift catalogs (see § 2.3.2 for details). MIPS upper limits are estimated from the 5σ upper limit of a detected MIPS source nearest the AzTEC/X-ray position (§ 2.3.2). Errors are given at the 1σ confidence level.

AzTEC ID	*Chandra* ID	1.4 GHz (μJy)	24 μm (μJy)	3.6 μm (μJy)	4.5 μm (μJy)	5.8 μm (μJy)	8.0 μm (μJy)	z_{spec}	z_{phot}
AzGN24	J123608.57+621435.8	45±9	51±6	6.4±0.6	9.5±0.8	13.4±1.3	18.3±1.5		
AzGN16a	J123615.83+621515.9	30±9	5±7	14.9±0.9	19.5±0.8	27.9±1.5	27.1±1.7		
AzGN16b	J123615.93+621522.0								
AzGN16c	J123616.08+621514.1	38±8	326±8	12.3±0.9	18.1±0.8	29.5±1.5	43.4±1.7	2.578	
AzGN10	J123627.52+621218.3	18±4	22±7	1.2±0.4	2.3±0.4	4.2±1.0	9.7±1.1		
AzGN11	J123635.86+620707.8	36±10	<38	4.6±1.5	5.6±1.5	10.5±2.0	22.0±2.0	0.952	
AzGN14	J123651.70+621221.7								
AzGN7a	J123711.32+621331.1	127±9	537±9	37.9±1.2	45.0±1.0	53.3±1.5	37.8±1.7	1.996	
AzGN7b	J123711.98+621325.8	52±8	219±7	9.2±0.9	11.4±0.8	16.1±1.3	12.3±1.5	1.996	
AzGN26	J123713.84+621826.2	652±5	55±6	3.5±0.6	6.0±0.5	9.4±1.3	16.6±1.5		
AzGN23	J123716.63+621733.4	381±8	1240±16	62.7±1.2	83.5±1.0	129.3±1.5	239.6±1.7	1.146	
AzGS29	J033158.25-274458.8		<80	73.7±0.1	49.0±0.2	37.0±1.0	19.9±1.0	0.575	0.579
AzGS8a	J033204.48-274643.3		7±4	3.6±0.1	3.5±0.1	1.3±0.6	1.9±0.7		1.450
AzGS8b	J033205.34-274644.0		164±5	13.4±0.1	15.7±0.1	20.6±0.6	27.5±0.6		
AzGS10	J033207.12-275128.6		26±8	5.5±0.2	5.7±0.2	6.9±1.2	4.8±1.0		0.990
AzGS38a	J033209.26-274240.9								
AzGS38b	J033209.71-274249.0	220±6	39±3	112.4±0.1	67.6±0.1	58.1±0.4	34.2±0.5	0.733	0.762
AzGS1	J033211.39-275213.7	32±6	122±5	10.4±0.1	14.6±0.1	20.0±0.6	28.2±0.7		
AzGS13	J033212.23-274620.9		224±4	53.7±0.1	42.7±0.1	33.1±0.4	31.9±0.5	1.033	1.030
AzGS7	J033213.88-275600.2	51±6	103±9	7.9±0.1	12.0±0.1	17.7±0.6	22.7±0.6		
AzGS11	J033215.32-275037.6	46±6	117±5	22.9±0.1	22.5±0.1	23.8±0.3	32.5±0.4	0.250	2.280[†]
AzGS17a	J033222.17-274811.6		200±5	11.8±0.1	16.5±0.1	23.9±0.3	20.9±0.4		2.500
AzGS17b	J033222.56-274815.0		62±7	16.9±0.1	20.2±0.1	26.3±0.3	21.2±0.4		2.660
AzGS34	J033229.46-274322.0		70±3	17.3±0.1	19.9±0.1	17.2±0.4	14.9±0.5		
AzGS20	J033234.78-275534.0							0.038	
AzGS14	J033235.18-275215.7		12±3	2.3±0.1	3.7±0.1	5.2±0.4	10.0±0.4		0.857
AzGS16	J033238.01-274401.2		46±3	5.0±0.1	8.1±0.1	10.9±0.4	16.4±0.5	1.401	1.180
AzGS18	J033244.02-274635.9		126±4	8.2±0.1	10.9±0.1	16.0±0.3	22.2±0.4	2.688	2.690
AzGS25	J033246.83-275120.9	90±6	140±4	13.9±0.1	18.8±0.1	24.5±0.4	32.2±0.5	1.101	1.330
AzGS9	J033302.94-275146.9	87±7	229±10	7.7±0.1	12.6±0.2	14.9±0.9	27.3±0.9		3.690
AzC56	J095905.05+022156.4		90±10	7.6±0.1	11.2±0.2	15.9±1.0	28.0±2.5		3.440
AzC181	J095929.70+021706.4		<930	39.0±0.2	44.9±0.3	39.8±1.0	26.3±2.4		1.700
AzC101	J095945.15+023021.1		300±20	78.1±0.2	58.2±0.3	44.9±1.1	44.4±2.4	0.893	0.870
AzC71	J095953.85+021853.6	79±11	520±20	52.0±0.2	49.2±0.3	56.9±1.1	44.4±2.6	0.853	0.720
AzC118	J095959.96+020633.1	104±13	220±20	22.2±0.1	23.0±0.2	22.1±1.0	41.5±2.1		0.790
AzC43	J100003.73+020206.4		<220	5.4±0.1	5.6±0.2	10.9±1.1	8.3±2.4		2.510
AzC81	J100006.11+015239.2		100±10	17.5±0.1	23.0±0.2	19.8±0.9	19.5±2.3	1.796	1.760
AzC45	J100006.55+023259.3		160±10	33.9±0.2	43.3±0.2	51.9±1.0	41.0±2.3		1.120
AzC44a	J100033.61+014902.0		160±20	71.8±0.6	61.0±0.5	47.2±1.1	44.8±2.2		0.910
AzC44b	J100033.75+014906.3								
AzC17	J100055.34+023441.1	78±12	1390±20	99.7±0.2	166.1±0.4	254.9±1.2	407.6±3.0	1.404	1.410
AzC147	J100107.46+015718.1		80±10	36.6±0.2	35.7±0.3	29.3±1.1	29.3±2.3		1.230
AzC108	J100116.15+023606.9		520±60	128.1±0.2	140.6±0.4	162.7±1.1	188.7±2.5	0.959	0.950
AzC85	J100139.73+022548.5	549±12	180±20	1100.3±2.3	780.2±2.0	510.3±2.1	346.1±3.0	0.124	0.120
AzC11	J100141.02+020404.8		210±20	11.2±0.1	16.3±0.2	26.5±1.0	40.9±2.3		

[†] The photometric redshift was adopted for J033215.32-275037.6 following cross-catalog comparison with GOODS-MUSIC (Santini et al. 2009) and additional analysis.

3.1.1 Model A: Absorbed Power-Law

Our first model provides a simple parametrization of the X-ray emission from an AGN, represented by a single power-law. The model includes the effects of both (Milky Way) Galactic and intrinsic absorption and is represented by the XSPEC model PHA(ZPHA(PO)). The X-ray spectra is thus defined by the intrinsic absorption, N_H, and photon index, Γ. As these values can be strongly correlated for weak sources, we chose to fix the photon index to $\Gamma = 1.8$, typical for unobscured AGNs (i.e. Nandra & Pounds 1994; Tozzi et al. 2006). The model (hereafter Model A) thus represents a typical AGN and provides an estimate of the level of obscuration present in our X-ray-identified SMGs.

3.1.2 Model B: Absorbed HMXB

Our second model (Model B) is developed for emission due to star formation and is based on the HMXB X-ray spectral
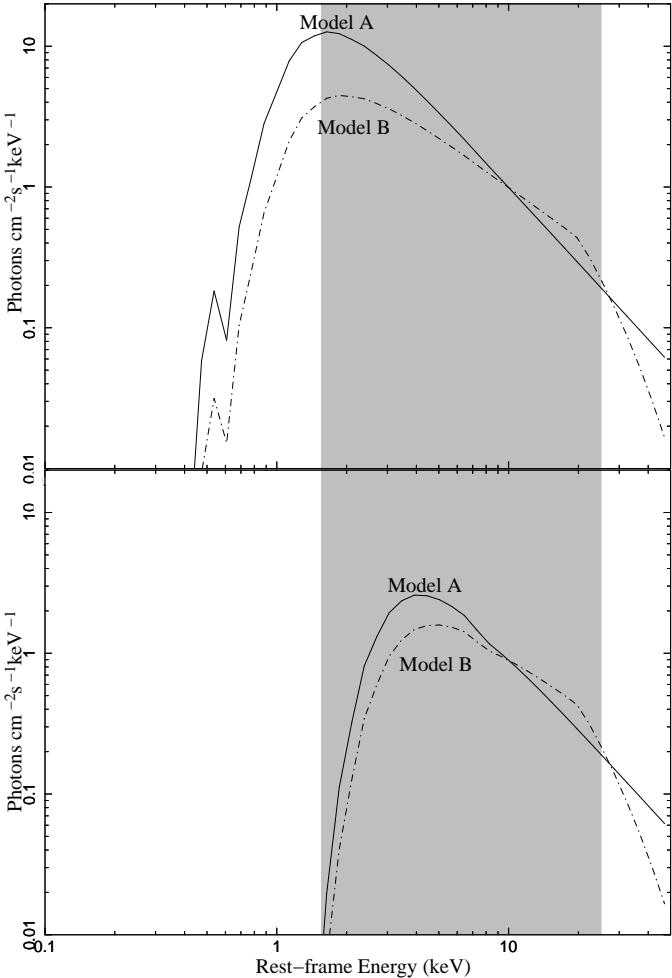
Figure 2. Comparison of the X-ray spectral Models A (solid) and B (dot-dashed) normalized at ∼10 keV. The models are shown for fiducial column densities of 10^{22} cm^{-2} (top) and 10^{23} cm^{-2} (bottom). The shaded region indicates the effective rest-frame energies sampled by the 0.5-8.0 keV observed spectrum of a source at $z \sim 2$.

model of Persic & Rephaeli (2002). In summary, the X-ray emission from HMXBs can be expressed as a broken power-law of the form

$$f(\epsilon) = \begin{cases} \epsilon^{-\Gamma_{acc}} & \text{if } \epsilon \leqslant \epsilon_c \\ \epsilon^{-\Gamma_{acc}} e^{-[\epsilon-\epsilon_c]/\epsilon_F} & \text{if } \epsilon > \epsilon_c \end{cases} \quad (1)$$

where Γ_{acc}=1.2 (typical of bright, accretion powered X-ray sources; White, Swank & Holt 1983) with a cutoff energy of $\epsilon_c \sim$20 keV and e-folding energy of $\epsilon_F \sim$12 keV. Ideally, when constructing a spectral model for stellar processes, we should also include contributions from low mass X-ray binaries (LMXBs) and supernovae. However, supernovae contribute little to > 2keV rest-frame flux compared to HMXBs. While LMXBs may contribute a considerable fraction of the hard X-ray flux, the low mass stellar companion typically has not had time to evolve off the main sequence and fill its Roche lobe by $z \sim$1-2. For sources in our sample with $z < 1$, we may still use the HMXB-SFR relation as Persic & Rephaeli (2007) showed that for moderate to high SFRs (SFRs$\gtrsim$50 M$_\odot$ yr^{-1}) the X-ray-SFR relation is similar to the HMXB-SFR relation. Our stellar spec-

tral model therefore consists of only the HMXB emission, which is absorbed by both Galactic and intrinsic material (PHA(ZPHA(HMXB)) in XSPEC, where the model HMXB is defined as given above). We include intrinsic obscuration in Model B, since it is clear from multi-wavelength evidence that SMGs are heavily dust-enshrouded systems. With Γ_{acc} fixed to 1.2, we are left with only the intrinsic obscuration and normalization to vary between spectra, similar to Model A.

As shown in Figure 2, there are immediate differences in the spectral shapes of our adopted models. Both models appear similar at low energies; however, the difference in spectral slopes, as well as the exponential cut-off in Model B, are apparent for higher energies. For high obscuration and low count spectra, it is difficult to distinguish between Model A and B (§ 3.1.3). However, the derived N_H values will vary according to the power-law spectral slope. Additionally, we can compare the X-ray-derived SFRs of Model B with those obtained through our NIR-to-radio SED modeling (§ 3.2).

3.1.3 *Application of X-ray Spectral Models*

We now apply our set of spectral models to the X-ray identified AzTEC SMGs. To correctly fit the intrinsic absorption, which has a strong energy dependence through the photo-electric cross-section, we require accurate source redshift information. This limits us to 32 out of our original sample of 45 X-ray sources (∼63 percent), including 5 sources in GOODS-N, 14 in GOODS-S, and 13 in COSMOS. We favor the spectroscopic redshift, whenever available, over the photometric redshift. Milky Way absorption values of 1.5, 0.9, and 2.5×10^{20} cm^{-2} are included for the spectra, depending on whether they were taken in GOODS-N, GOODS-S, or COSMOS, respectively. The best-fit parameters for each set of models, as well as their C-statistic values and associated rest-frame, absorption corrected 2.0-10.0 keV luminosities, are given in Table 3. As a simple check, we have compared our derived luminosities with those of previously published catalogs (i.e. Alexander et al. 2003; Tozzi et al. 2006) which correlate well with our results.

In order to determine which of our sets of models offer the best fit to the X-ray spectra, we run 2000 Monte Carlo simulations through the GOODNESS command in XSPEC, which provides the percentage of simulations that have a C-statistic lower than the observed spectrum. The best-fit spectral models, the ones providing the lowest goodness fraction, have been highlighted in boldface in Table 3. As one might expect, the models with the lowest C-statistics tend to also provide the lowest goodness fractions, indicating a very high probability that the observed spectrum can be characterized by the best-fit model. Models A and B often show very similar C-statistics, which leads to only a few percent difference in their goodness fractions. These differences are *not* statistically significant based on 10000 FAKEIT simulated fits using an intrinsically absorbed Γ=1.8 power-law as the template spectrum.

We find that ∼53 percent (17/32) of the AzTEC/X-ray sources have X-ray spectra that immediately favors an AGN origin. Of these, ∼70 percent show evidence for heavy obscuration with $N_H \gtrsim 10^{23}$ cm^{-2}. Regardless of the best-fit spectral model, the majority of AzTEC/X-ray sources (22/32) have 2.0 to 10.0 keV rest-frame luminosi-

Table 3. X-ray spectral fits to identified AzTEC/X-ray sources. Spectral models used are: Galactic dust- and intrinsically-absorbed AGN power-law (PHA(ZPHA(PO)), Model A) and Galactic dust- and intrinsically-absorbed power-law with an exponential cut-off relating to emission from HMXBs (PHA(ZPHA(HMXB)), Model B). Models that offer the best fit to the X-ray spectra based on our simulations are emphasized in bold. The relevant parameters given here are the intrinsic neutral hydrogen column density (N_H in 10^{22} cm^{-2}); absorption corrected, rest-frame X-ray luminosity in the 2.0-10.0 keV energy band (L_X in 10^{43} ergs s^{-1}) and X-ray derived SFR (SFR_X in 1000 $M_\odot$ yr^{-1}) for Model B assuming the P04 relation. Errors are given at the 90 percent confidence level.

Chandra ID	Γ_{Eff}	Model A			Model B			
		N_H	L_X	C-stat	N_H	L_X	SFR_X	C-stat
J123616.08+621514.1	$0.98^{+0.23}_{-0.28}$	$16.46^{+7.64}_{-6.20}$	4.40	159.3	**$6.70^{+5.76}_{-4.05}$**	**2.60**	**26.0**	**161.0**
J123635.86+620707.8	$-0.56^{+0.36}_{-0.45}$	$97.94^{+25.89}_{-29.10}$	8.89	212.7	**$74.19^{+25.15}_{-27.01}$**	**4.51**	**45.1**	**213.3**
J123711.32+621331.1	$0.69^{+0.52}_{-0.55}$	$9.72^{+21.27}_{-6.95}$	0.92	189.0	**< 16.28**	**0.62**	**6.2**	**186.7**
J123711.98+621325.8	$-0.41^{+0.65}_{-0.61}$	$57.60^{+45.78}_{-24.30}$	2.70	199.2	**$38.31^{+37.00}_{-18.49}$**	**1.37**	**13.7**	**198.8**
J123716.63+621733.4	$1.17^{+0.05}_{-0.06}$	**$2.10^{+0.25}_{-0.23}$**	**9.95**	**236.6**	$0.52^{+0.18}_{-0.17}$	8.76	87.6	239.4
J033158.25-274458.8	$0.99^{+0.59}_{-0.55}$	< 1.93	0.07	177.3	**< 0.83**	**0.08**	**0.8**	**173.8**
J033204.48-274643.3	$1.39^{+0.24}_{-0.20}$	**$1.00^{+1.02}_{-0.82}$**	**1.08**	**187.0**	< 0.37	1.07	10.7	186.1
J033207.12-275128.6	$0.74^{+-0.75}_{-0.75}$	< 14.0	0.04	189.1	< 12.3	0.04	0.4	189.2
J033209.71-274249.0	$2.22^{+0.30}_{-0.28}$	< 0.06	0.25	199.4	< 0.04	0.34	3.4	238.4
J033212.23-274620.9	$0.85^{+0.15}_{-0.13}$	$3.34^{+0.69}_{-0.68}$	1.00	189.8	**$1.53^{+0.58}_{-0.50}$**	**0.88**	**8.8**	**186.6**
J033215.32-275037.6	$0.96^{+0.40}_{-0.29}$	**$0.82^{+0.41}_{-0.42}$**	**0.01**	**204.2**	$0.34^{+0.35}_{-0.31}$	0.01	0.1	205.7
J033222.17-274811.6	$0.38^{+0.27}_{-0.28}$	$39.19^{+14.60}_{-10.40}$	3.11	181.8	**$23.67^{+10.86}_{-8.72}$**	**1.66**	**16.6**	**182.1**
J033222.56-274815.0	$-0.43^{+0.49}_{-0.42}$	$94.11^{+55.73}_{-32.70}$	3.51	182.9	**$55.83^{+45.48}_{-21.71}$**	**1.49**	**14.9**	**180.6**
J033234.78-275534.0	$1.06^{+0.28}_{-0.31}$	$0.43^{+0.27}_{-0.19}$	4.0e-4	167.9	< 0.45	**5.0e-4**	**5.0e-3**	167.7
J033235.18-275215.7	$0.64^{+0.39}_{-0.54}$	**$5.17^{+4.38}_{-2.08}$**	**0.12**	**179.7**	$3.17^{+3.36}_{-1.84}$	0.10	1.0	180.9
J033238.01-274401.2	$1.77^{+1.00}_{-0.88}$	**< 5.53**	**0.14**	**235.8**	< 3.95	0.14	1.4	237.6
J033244.02-274635.9	$2.01^{+0.20}_{-0.20}$	**< 0.96**	**3.64**	**181.6**	< 0.26	3.15	31.5	230.3
J033246.83-275120.9	$0.95^{+0.52}_{-0.64}$	$4.32^{+4.92}_{-3.16}$	0.20	209.2	**< 5.64**	**0.17**	**1.7**	**208.9**
J033302.94-275146.9	$1.41^{+0.37}_{-0.26}$	**$10.36^{+10.41}_{-6.34}$**	**14.37**	**175.5**	< 7.89	8.69	86.9	182.4
J095905.05+022156.4	$0.98^{+1.40}_{-1.25}$	**< 78.54**	**4.92**	**47.1**	< 60.47	2.72	27.2	47.6
J095929.70+021706.4	$1.11^{+1.43}_{-1.23}$	< 4.14	0.83	92.7	**< 3.28**	**0.93**	**9.3**	**91.8**
J095945.15+023021.1	$1.24^{+2.97}_{-1.38}$	< 1.01	0.41	140.0	**< 0.95**	**0.57**	**5.7**	**139.7**
J095953.85+021853.6	$0.57^{+0.58}_{-0.59}$	$5.56^{+3.98}_{-3.14}$	0.79	103.2	**$3.27^{+3.66}_{-2.56}$**	**0.66**	**6.6**	**103.7**
J095959.96+020633.1	$0.52^{+0.66}_{-0.74}$	**$5.53^{+4.30}_{-3.11}$**	**0.39**	**79.0**	$3.71^{+3.92}_{-2.65}$	0.33	3.3	80.0
J100003.73+020206.4	$1.00^{+2.06}_{-1.53}$	**< 124.89**	**6.16**	**141.2**	< 82.08	2.52	25.2	140.8
J100006.11+015239.2	$1.77^{+0.70}_{-0.57}$	**< 1.48**	**2.25**	**115.6**	< 0.83	2.26	22.6	118.3
J100006.55+023259.3	$1.26^{+0.58}_{-0.54}$	**< 2.98**	**0.82**	**87.1**	< 1.56	0.79	7.9	86.4
J100033.61+014902.0	$1.57^{+0.50}_{-0.45}$	< 0.68	0.75	104.8	**< 0.29**	**0.95**	**9.5**	**107.5**
J100055.34+023441.1	$1.85^{+0.19}_{-0.19}$	< 0.44	**24.88**	159.2	< 0.10	26.84	268.4	181.6
J100107.46+015718.1	$1.59^{+0.79}_{-0.60}$	$0.88^{+2.27}_{-0.86}$	1.46	148.5	**< 1.50**	**1.49**	**14.9**	**149.9**
J100116.15+023606.9	$1.72^{+0.60}_{-0.56}$	**$0.20^{+1.31}_{-0.19}$**	**5.84**	**100.3**	< 0.69	6.72	67.1	102.6
J100139.73+022548.5	$3.23^{+0.79}_{-0.71}$	**< 0.05**	**0.01**	**81.3**	< 0.04	0.02	0.2	97.5

ties of $\gtrsim 10^{43}$ ergs s^{-1}, heavily favoring an AGN interpretation. Note that the derived luminosities are sensitive to the choice of the X-ray model. For those AzTEC/X-ray sources that favor the starburst model Model B, we use the X-ray luminosity to SFR relation of P04 to estimate a SFR, assuming no contribution from a buried AGN. There is some uncertainty in the exact form of the X-ray-to-SFR scaling relation as discussed by Mineo, Gilfanov, & Sunyaev (2011); however, many of these relations consider local, low SFR ($\lesssim 10$ $M_\odot$ yr^{-1}) sources during their construction. As we are concerned with potentially high SFRs, we favor the P04 and Persic & Rephaeli (2007) SFR-X-ray scaling relations; using the Ranalli et al. (2003) relation, or similar, would decrease the estimated SFRs by a factor of ~2-5. The high X-ray luminosities would require very strong SFRs on the order of $\gtrsim 10^3 - 10^4$ $M_\odot$ yr^{-1}, which is pushing the limits for typical SMGs. However, there are 5 sources with $L_X \lesssim 10^{42}$ ergs s^{-1} which are candidates to be starburst powered X-ray sources. These sources account for ~16 per-

cent of our X-ray-identified SMG sample; consistent with the starburst-powered fraction of LNPS10 (~17±6 percent). We caution, however, that this does not necessarily imply that their X-ray emission is dominated by star formation (see § 3.2.2, Tables 4). These results thus show that the bulk of the X-ray emission from our SMG sample is predominately produced by obscured AGNs.

3.2 NIR-to-Radio SED Modeling

For an alternative view of the AGN and star formation contributions, we now examine the near-IR-to-radio SEDs of the AzTEC/X-ray sources. To be luminous at (sub-)millimetre wavelengths, a source must contain dust heated to T~30K (Chapman et al. 2005; Pope et al. 2006) through some central engine. While it is possible to have (sub-)mm emission due to synchrotron processes from radio-loud AGN (e.g., Vieira et al. 2010), the corresponding radio fluxes would have to be significantly larger (on order 1-100 mJy;

de Zotti et al. 2010; Vieira et al. 2010) than those observed for our AzTEC/X-ray sources, which range from 0.02 to 0.65 mJy (Table 2). The required dust heating must then be accomplished either by star formation, AGN activity, or some combination of the two.

For our SED modeling, we consider the templates of Efstathiou, Rowan-Robinson & Siebenmorgen (2000) and Siebenmorgen et al. (2004) to parametrize emission from a starburst (SB) and AGN component, respectively. This selection of templates is widely used in the literature and has shown to provide reasonable results to similar classes of sources over the NIR-to-mm wavelength regime (i.e. Efstathiou, Rowan-Robinson & Siebenmorgen 2000; Siebenmorgen et al. 2004; Meng et al. 2010; Serra et al. 2011; Younger & Hopkins 2011; Yun et al. 2012, and references therein). For this work, we favor the Siebenmorgen et al. (2004) AGN models as opposed to torus models as we are more interested in the integrated AGN host properties rather than the centralized nuclear region. Additionally, these models are built from basic radiative transfer models, incorporating relevant dust emission/absorption physics, with simple parametrizations comparable to the SB models.

In order to estimate the total SED, we apply a simple linear combination of the two template sets. Since this approach may introduce strong template-parameter degeneracies into our summed SEDs, we use a Monte Carlo Markov Chain (MCMC) technique to perform the fitting. While computationally slower compared to direct maximum likelihood (least squares) fitting, MCMC has the advantage that the full set of posterior parameter distributions are returned - allowing for direct inspection of the posteriors for degeneracies that may bias our interpretations of the fits (see Figure 4). The full details of this method will be presented in Johnson et al. (in prep). Here, we briefly describe the adopted models and their implications on the AzTEC/X-ray source population.

3.2.1 SED Models and Fitting

Before applying the SED templates to the observed SEDs, it is helpful to have an understanding of how the templates parametrize the underlying physics and resulting IR emission. In the Efstathiou, Rowan-Robinson & Siebenmorgen (2000) templates, emission from a dusty starburst is traced from a single star forming GMC with the cloud optical depth (τ_ν) and starburst age setting the overall shape of the SED. Specifically, τ_ν controls the strength of the PAH and silicate features, while older starburst ages shift the IR peak to longer wavelengths. A normalization factor is then required to scale the emission from a single GMC to the full system. This normalization is comparable to the SFR at the onset of the burst as Efstathiou, Rowan-Robinson & Siebenmorgen (2000) assume an exponentially decaying SFR history of the form

$$SFR(t) \approx SFR(0)e^{-t/20 \text{ Myr}} \qquad (2)$$

where t is the SB age; SFR estimates obtained this way are approximately 2-3 times lower than more traditional FIR SFR indicators – for example, the Kennicutt (1998) relation. The AGN models are described by a single cen-

tral illuminating source with intrinsic luminosity L surrounded by a spherical dust distribution of size R and the visual extinction (A_V). The dust distribution, temperature, strength of absorption/emission lines, etc. are adjusted through a combination of the size and visual extinction. It should be noted that the Siebenmorgen et al. (2004) AGN templates make a number of simplifications compared to alternative AGN models. Modern AGN templates (e.g. Fritz, Franceshini & Hatziminiaoglou 2006; Nenkova et al. 2008, and references therein) consider the AGN to be surrounded by torus, generally composed of a clumpy material, whose geometry flares outward. This geometry naturally falls in line with the standard AGN unified model where looking through the torus results in Type 2 (obscured) AGN while Type 1 (unobscured) AGN are produced from 'face-on' observations. The Siebenmorgen et al. (2004) models obviously lack the asymmetry and clumpy distribution of the traditional AGN torus but are able to recreate the same effects; Siebenmorgen et al. comments that it is the dust mass and distance from the source (set by A_V and R) that are most important. Though torus geometries may extend to the kpc scale (e.g. Granato & Danese 1994; Fritz, Franceshini & Hatziminiaoglou 2006; Nenkova et al. 2008) and can produce significant cold dust emission, they lack the dust intrinsic to the host galaxy, whose geometry extends well beyond that of a nuclear torus. Given that the photometry for our sample can not resolve our sources, we believe the Siebenmorgen et al. (2004) models to be better representative of galactic emission resulting from an AGN than the traditional torus models.

Using the above models, we have three to six free parameters with 6-7 available SED data points per AzTEC/X-ray source. In our fitting, we are able to predict an X-ray luminosity from the FIR luminosity/SFR using the relations of Marconi et al. (2004) and P04 for the AGN and SB models, respectively. This allows us to then use the observed X-ray luminosities in Table 3 as an additional prior to the fits. As the SB models do not account for any radio emission, we employ the radio-FIR correlation of Yun, Reddy & Condon (2001) to add a radio 'tail' to the templates. Note, however, that this may still pose some uncertainty when combining templates as there is scatter in this relationship (e.g. Carilli & Yun 2000; Chapman et al. 2005) and it does not predict any radio emission resulting from an AGN.

In fitting the near-IR-to-radio SEDs of our X-ray-detected SMGs, we consider two combinations of the SED templates: (1) AGN and SB templates including the observed X-ray luminosity and X-ray-absorbing column density as priors to the AGN luminosity, SB SFR and AGN A_V and (2) SB only without the additional X-ray constraints. The first set of models serves to estimate the AGN contribution to the bolometric and 1.1 mm emission. The SB only fits provide a measure of the necessity of the AGN templates. The X-ray luminosity prior had to be excluded for these fits as their inclusion produced unreasonable results (see § 3.2.2). Tables 4 and 6 and Figure 3 show the results of our MCMC fitting technique to our AzTEC/X-ray sample. For each set of best-fit parameters, we calculate the log of the likelihood, ln(L); higher values of ln(L) indicate a higher probability that the data is consistent with the best-fit model.

Table 4. Best-fit parameters for the composite AGN+SB models based on the broadband photometry of AzTEC/X-ray sources. The predicted X-ray luminosities are compared to those derived from the X-ray spectral modeling (§ 3.1.4) to provide additional weights in calculating the likelihoods. Errors are given at the 1σ confidence level after marginalizing over all other free parameters in the fitted templates. Col.(1): *Chandra* Source ID. Col.(2), (3), and (4): AGN template galaxy outer radius, intrinsic luminosity and visual extinction. Col.(5), (6), and (7): SB template normalization, age, and optical depth.

Chandra ID	AGN R kpc	L log(L$_\odot$)	A$_V$ mag	Norm	SB Age Myr	τ_ν
(1)	(2)	(3)	(4)	(5)	(6)	(7)
J123616.08+621514.1	$0.13^{+0.15}_{-0.01}$	$11.51^{+0.05}_{-0.18}$	$26.10^{+36.73}_{-17.57}$	$8532.40^{+650.39}_{-490.44}$	$44.95^{+11.53}_{-7.68}$	$192.73^{+7.26}_{-41.29}$
J123635.86+620707.8	$14.30^{+1.70}_{-14.17}$	$10.52^{+0.11}_{-0.18}$	$125.85^{+2.14}_{-124.84}$	$213.66^{+114.63}_{-92.54}$	$56.24^{+15.75}_{-28.36}$	$196.40^{+3.60}_{-139.53}$
J123711.32+621331.1	$0.91^{+15.07}_{-0.79}$	$10.41^{+0.11}_{-0.12}$	$56.00^{+31.97}_{-54.99}$	$7965.80^{+182.33}_{-211.12}$	$56.66^{+6.41}_{-10.49}$	$198.62^{+1.37}_{-43.97}$
J123711.98+621325.8	$9.20^{+6.74}_{-9.08}$	$10.81^{+0.13}_{-0.14}$	$74.24^{+53.54}_{-73.24}$	$2685.09^{+113.89}_{-287.82}$	$43.46^{+12.53}_{-5.76}$	$195.49^{+4.51}_{-42.44}$
J123716.63+621733.4	$15.98^{+0.02}_{-7.55}$	$12.25^{+0.02}_{-0.01}$	$2.10^{+1.80}_{-1.02}$	$9451.94^{+241.06}_{-179.17}$	$1.37^{+4.85}_{-1.37}$	$151.18^{+46.25}_{-47.75}$
J033158.25-274458.8	$14.26^{+1.74}_{-14.13}$	$9.21^{+0.20}_{-0.13}$	$1.00^{+3.91}_{-0.01}$	$1097.69^{+2.81}_{-4.57}$	$70.67^{+1.33}_{-6.40}$	$199.88^{+0.11}_{-48.26}$
J033204.48-274643.3	$14.63^{+1.36}_{-14.49}$	$10.67^{+0.16}_{-0.19}$	$1.03^{+9.78}_{-0.03}$	$233.46^{+96.74}_{-53.53}$	$68.27^{+3.73}_{-10.70}$	$105.65^{+94.31}_{-55.34}$
J033207.12-275128.6	$8.48^{+7.51}_{-8.35}$	$8.97^{+0.11}_{-0.13}$	$67.61^{+7.31}_{-66.61}$	$246.75^{+13.02}_{-24.16}$	$71.54^{+0.45}_{-13.85}$	$197.10^{+2.88}_{-44.25}$
J033209.71-274249.0	$15.91^{+0.09}_{-5.84}$	$11.00^{+0.01}_{-0.01}$	$1.00^{+0.01}_{-0.01}$	$2040.88^{+3.22}_{-3.52}$	$71.22^{+0.78}_{-0.50}$	$198.51^{+1.48}_{-31.29}$
J033212.23-274620.9	$15.91^{+0.09}_{-7.64}$	$11.25^{+0.01}_{-0.01}$	$1.08^{+0.89}_{-0.08}$	$2106.95^{+8.74}_{-6.94}$	$71.46^{+0.54}_{-7.25}$	$193.54^{+6.45}_{-42.36}$
J033215.32-275037.6	$5.65^{+10.34}_{-5.53}$	$10.70^{+0.05}_{-0.29}$	$1.03^{+1.99}_{-0.03}$	$3280.00^{+23.15}_{-27.60}$	$70.60^{+1.40}_{-6.14}$	$50.31^{+47.39}_{-0.30}$
J033222.17-274811.6	$15.38^{+0.62}_{-15.11}$	$11.27^{+0.07}_{-0.02}$	$4.46^{+10.92}_{-2.38}$	$2483.75^{+80.91}_{-22.82}$	$44.38^{+11.97}_{-6.94}$	$53.72^{+43.88}_{-3.72}$
J033222.56-274815.0	$13.81^{+2.19}_{-13.68}$	$10.85^{+0.19}_{-0.08}$	$1.08^{+2.24}_{-0.08}$	$3844.91^{+37.39}_{-72.25}$	$71.97^{+0.03}_{-7.59}$	$57.91^{+40.71}_{-7.88}$
J033235.18-275215.7	$0.15^{+0.10}_{-0.02}$	$9.76^{+0.02}_{-0.01}$	$50.82^{+1.18}_{-18.32}$	$109.77^{+0.02}_{-6.44}$	$71.98^{+0.02}_{-7.41}$	$198.63^{+1.37}_{-46.96}$
J033238.01-274401.2	$15.69^{+0.31}_{-15.56}$	$9.51^{+0.07}_{-0.15}$	$10.90^{+19.09}_{-9.90}$	$1019.35^{+22.35}_{-21.65}$	$36.06^{+8.06}_{-8.69}$	$198.61^{+1.39}_{-43.73}$
J033244.02-274635.9	$0.13^{+0.11}_{-0.01}$	$11.51^{+0.04}_{-0.01}$	$5.92^{+0.08}_{-1.70}$	$2523.09^{+38.84}_{-38.49}$	$57.21^{+6.09}_{-11.43}$	$101.31^{+45.07}_{-46.64}$
J033246.83-275120.9	$0.14^{+0.11}_{-0.01}$	$10.00^{+0.02}_{-0.01}$	$30.97^{+0.03}_{-14.38}$	$868.22^{+9.67}_{-7.11}$	$71.34^{+0.66}_{-6.77}$	$197.29^{+2.71}_{-45.44}$
J033302.94-275146.9	$0.25^{+0.22}_{-0.01}$	$12.26^{+0.03}_{-0.01}$	$6.96^{+8.01}_{-2.80}$	$7001.07^{+139.78}_{-215.29}$	$44.91^{+11.39}_{-7.35}$	$100.74^{+45.91}_{-46.93}$
J095905.05+022156.4	$2.39^{+13.57}_{-2.26}$	$11.40^{+0.13}_{-0.13}$	$7.42^{+120.08}_{-6.42}$	$8693.26^{+308.01}_{-550.64}$	$44.42^{+11.06}_{-6.48}$	$151.03^{+44.55}_{-47.51}$
J095929.70+021706.4	$6.22^{+9.78}_{-6.09}$	$10.61^{+0.12}_{-0.13}$	$16.33^{+1.22}_{-15.32}$	$4819.83^{+39.78}_{-238.62}$	$71.79^{+0.21}_{-12.12}$	$148.38^{+48.37}_{-44.31}$
J095945.15+023021.1	$9.82^{+6.00}_{-8.78}$	$10.75^{+0.01}_{-0.01}$	$1.31^{+0.68}_{-0.31}$	$1797.01^{+8.54}_{-19.38}$	$71.87^{+0.13}_{-7.66}$	$60.11^{+38.85}_{-10.11}$
J095953.85+021853.6	$0.13^{+0.11}_{-0.01}$	$10.52^{+0.08}_{-0.01}$	$31.08^{+5.99}_{-14.31}$	$1677.68^{+15.21}_{-14.04}$	$71.88^{+0.12}_{-7.63}$	$195.74^{+4.25}_{-44.40}$
J095959.96+020633.1	$12.49^{+3.50}_{-12.37}$	$10.09^{+0.07}_{-0.02}$	$52.38^{+0.20}_{-33.85}$	$669.15^{+7.07}_{-11.74}$	$46.63^{+8.96}_{-9.36}$	$190.37^{+9.63}_{-39.41}$
J100003.73+020206.4	$12.25^{+3.75}_{-12.12}$	$11.18^{+0.11}_{-0.17}$	$121.10^{+6.90}_{-120.08}$	$995.74^{+44.76}_{-169.08}$	$70.55^{+1.45}_{-24.73}$	$54.92^{+43.17}_{-4.92}$
J100006.11+015239.2	$12.59^{+3.41}_{-12.47}$	$11.07^{+0.13}_{-0.16}$	$7.90^{+0.02}_{-6.89}$	$2859.00^{+34.58}_{-188.34}$	$71.82^{+0.18}_{-13.53}$	$185.32^{+14.67}_{-33.72}$
J100006.55+023259.3	$0.92^{+2.81}_{-0.75}$	$10.43^{+0.07}_{-0.11}$	$1.01^{+0.93}_{-0.01}$	$1905.42^{+19.50}_{-16.07}$	$71.04^{+0.96}_{-6.52}$	$194.34^{+5.66}_{-42.19}$
J100033.61+014902.0	$6.84^{+9.16}_{-5.87}$	$10.64^{+0.13}_{-0.12}$	$1.47^{+0.09}_{-0.34}$	$2418.84^{+26.17}_{-41.92}$	$71.81^{+0.19}_{-7.48}$	$193.21^{+6.79}_{-41.24}$
J100055.34+023441.1	$15.73^{+0.26}_{-7.54}$	$12.75^{+0.02}_{-0.01}$	$2.32^{+0.03}_{-0.31}$	$1366.06^{+69.89}_{-49.88}$	$17.24^{+8.42}_{-6.91}$	$54.57^{+43.64}_{-4.57}$
J100107.46+015718.1	$15.60^{+0.40}_{-12.86}$	$10.87^{+0.25}_{-0.08}$	$2.43^{+5.60}_{-1.42}$	$2202.64^{+101.75}_{-130.42}$	$70.94^{+1.06}_{-6.85}$	$197.34^{+2.66}_{-46.46}$
J100116.15+023606.9	$0.13^{+0.11}_{-0.01}$	$11.82^{+0.11}_{-0.15}$	$8.08^{+0.01}_{-0.07}$	$4426.14^{+18.13}_{-15.78}$	$64.22^{+7.29}_{-6.83}$	$196.37^{+3.62}_{-43.90}$
J100139.73+022548.5	$0.99^{+0.32}_{-0.48}$	$9.00^{+0.01}_{-0.01}$	$1.00^{+0.01}_{-0.01}$	$10.41^{+0.08}_{-0.09}$	$2.07^{+4.26}_{-2.07}$	$51.98^{+44.46}_{-1.96}$

3.2.2 SED Fitting Results

Figure 3 shows that our method is able to produce reasonable fits to the AzTEC/X-ray sources; the source J033234.78-274815.0 was excluded as it has no discernible IRAC/MIPS counterpart despite having a spectroscopic redshift (see Table 2). While the majority (∼87 percent) of our sources can be fit using the SB templates alone, they typically under-predict the 1.1 mm emission, recovering on average ∼30-38 percent of the observed flux. Including the AGN models helps to slightly increase the model fluxes and are generally required to match the X-ray luminosity prior but are still unable to match the mm-wavelength observations; contributing little, if at all, to the bolometric luminosities and observed 1.1 mm flux. In some cases (e.g. J033212.23-274620.9), the AGN and SB templates appear very similar in the final fit. This likely results from the similarities in the dust treatment and radiative transfer in the templates as noted by Siebenmorgen & Efstathiou (2005) for

effectively identical template parameters (i.e. dust content, optical depth and intrinsic luminosity; see also their figure 4). In many cases, the fit values for AGN R and A$_V$ are rather poor and show a large range in acceptable values. This effect stems from our use of the X-ray luminosity prior which effectively sets the AGN bolometric luminosity, preventing any additional AGN contribution to the bolometric SED and thus leading to unconstrained R and A$_V$ (see also Figure 5). The fact that A$_V$ had such poor constraints prompted us to include the X-ray column density to avoid over-estimating the dust content. By virtue of our MCMC technique, we may readily identify any degeneracies between the AGN and SB template sets; however, Figure 4 shows that there are no large parameter-parameter degeneracies, although some parameters are not very well constrained. This is particularly the case for AGN R and A$_V$ as mentioned above.

Due to the under-prediction of the 1.1 mm flux, we are biased to under estimate the total IR luminosity such that the values reported in Table 4 are more likely to be lower

Table 5. Continuation of Table 4 containing the derived physical properties based on the fitted parameters. Col.(1): *Chandra* Source ID. Col.(2): Total model-derived, rest-frame bolometric IR luminosity from the AGN and SB templates over the wavelength range ∼0.001-1500μm. Col.(3): SFR derived from Eqn. 2 (§ 3.2.1) and Cols. 5 & 6 of Table 4. Col.(4): SED derived X-ray luminosity. Col.(5): Fractional contribution of AGN template to total model emission at 1.1mm. Col.(6): Fractional contribution of model to observed 1.1mm flux. Col.(7): ln(L) of best-fit parameters.

Chandra ID	IR Lum. $10^{12}L_\odot$	SFR $M_\odot\ yr^{-1}$	X-ray Lum. $10^{43}ergs\ s^{-1}$	$f_{AGN,1.1mm}$	$f_{1.1mm}$	ln(L)
(1)	(2)	(3)	(4)	(5)	(6)	(7)
J123616.08+621514.1	$11.10^{+3.30}_{-3.20}$	901	$4.84^{+0.57}_{-1.26}$	0.00	0.001	-27.94
J123635.86+620707.8	$0.23^{+0.33}_{-0.11}$	12	$0.79^{+0.19}_{-0.21}$	0.91	0.312	-11.40
J123711.32+621331.1	$7.10^{+2.61}_{-1.21}$	468	$0.72^{+0.13}_{-0.14}$	0.01	0.005	-40.04
J123711.98+621325.8	$3.64^{+0.65}_{-1.22}$	305	$1.39^{+0.34}_{-0.31}$	0.16	0.059	-9.59
J123716.63+621733.4	$13.00^{+15.90}_{-0.20}$	8825	$17.30^{+0.63}_{-0.11}$	0.23	0.131	-2868.31
J033158.25-274458.8	$0.67^{+0.12}_{-0.03}$	32	$0.07^{+0.03}_{-0.01}$	0.05	0.017	-2226.84
J033204.48-274643.3	$0.20^{+0.07}_{-0.06}$	7	$1.05^{+0.35}_{-0.33}$	0.44	0.021	-24.87
J033207.12-275128.6	$0.15^{+0.06}_{-0.01}$	6	$0.04^{+0.01}_{-0.01}$	0.25	0.010	-23.65
J033209.71-274249.0	$1.32^{+0.02}_{-0.03}$	57	$1.87^{+0.01}_{-0.01}$	0.10	0.070	-135568.62
J033212.23-274620.9	$1.43^{+0.26}_{-0.02}$	59	$2.94^{+0.02}_{-0.01}$	0.11	0.038	-3350.01
J033215.32-275037.6	$2.04^{+0.34}_{-0.10}$	96	$1.10^{+0.09}_{-0.44}$	0.01	0.004	-1280.28
J033222.17-274811.6	$3.39^{+0.78}_{-0.97}$	269	$3.08^{+0.46}_{-0.13}$	0.18	0.098	-60.08
J033222.56-274815.0	$2.32^{+0.51}_{-0.01}$	105	$1.48^{+0.56}_{-0.22}$	0.04	0.022	-62.72
J033235.18-275215.7	$0.07^{+0.02}_{-0.01}$	3	$0.18^{+0.01}_{-0.01}$	0.02	0.000	-302.13
J033238.01-274401.2	$1.70^{+0.50}_{-0.38}$	167	$0.13^{+0.02}_{-0.03}$	0.10	0.024	-111.65
J033244.02-274635.9	$2.53^{+0.92}_{-0.35}$	144	$4.75^{+0.44}_{-0.16}$	0.00	0.000	-89.91
J033246.83-275120.9	$0.53^{+0.10}_{-0.01}$	24	$0.30^{+0.01}_{-0.01}$	0.00	0.000	-4001.74
J033302.94-275146.9	$10.70^{+2.30}_{-2.60}$	741	$17.39^{+1.32}_{-0.25}$	0.00	0.001	-61.65
J095905.05+022156.4	$11.40^{+2.60}_{-3.30}$	942	$4.08^{+0.93}_{-0.88}$	0.01	0.009	-4.53
J095929.70+021706.4	$2.87^{+0.94}_{-0.06}$	133	$0.97^{+0.21}_{-0.22}$	0.06	0.027	-2.33
J095945.15+023021.1	$1.11^{+0.23}_{-0.01}$	49	$1.19^{+0.04}_{-0.01}$	0.04	0.007	-588.57
J095953.85+021853.6	$1.02^{+0.22}_{-0.01}$	46	$0.78^{+0.15}_{-0.03}$	0.00	0.000	-222.44
J095959.96+020633.1	$0.82^{+0.27}_{-0.19}$	65	$0.36^{+0.05}_{-0.02}$	0.51	0.085	-174.35
J100003.73+020206.4	$0.76^{+0.56}_{-0.11}$	29	$2.65^{+0.58}_{-0.74}$	0.75	0.212	-18.55
J100006.11+015239.2	$1.80^{+0.64}_{-0.09}$	78	$2.21^{+0.57}_{-0.56}$	0.21	0.063	-11.98
J100006.55+023259.3	$1.17^{+0.21}_{-0.04}$	54	$0.68^{+0.07}_{-0.13}$	0.00	0.000	-4319.74
J100033.61+014902.0	$1.47^{+0.31}_{-0.03}$	66	$1.00^{+0.23}_{-0.21}$	0.03	0.005	-323.60
J100055.34+023441.1	$9.53^{+0.69}_{-0.73}$	576	$40.84^{+1.98}_{-0.37}$	0.47	0.076	-18184.24
J100107.46+015718.1	$1.40^{+0.31}_{-0.06}$	63	$1.52^{+0.86}_{-0.23}$	0.12	0.028	-93.88
J100116.15+023606.9	$3.85^{+0.71}_{-0.63}$	178	$8.23^{+1.68}_{-1.96}$	0.00	0.000	-1096.50
J100139.73+022548.5	$0.01^{+0.02}_{-0.01}$	9	$0.04^{+0.01}_{-0.01}$	0.32	0.001	-187114.26

limits. Correcting for the under-prediction, we can expect the luminosities to be ∼2-3 times higher. As a result, the FIR-derived SFRs and the associated SFR-derived X-ray luminosities for J033215.32-275037.6 and J033207.12-275128.6 are more likely to be in line with their observed X-ray luminosities. The remaining starburst-candidate X-ray sources (J033158.25-274458.8 and J100139.73+022548.5) are still ambiguous as their X-ray derived SFRs are ∼5-8× higher than their IR counterparts; however, the poor fits to these sources prevents an accurate measurement of their FIR luminosity and SFR, hindering our interpretation. Nevertheless, it remains plausible that at least ∼6 percent of our X-ray-detected SMGs are starburst-dominated in both the IR and X-ray with little (if any) emission due to an AGN.

It is possible to account for the missing 1.1 mm flux if we relax the constraints on many of the fit parameters. For instance, the SB models can provide a better fit if we relax the redshift prior. Similarly, if the X-ray luminosity constraint is removed then the AGN templates can account for the remaining 1.1 mm flux with significantly more dust (as set by A_V and R). These fits, however, are completely unphysical either due to inaccurate redshifts ($\Delta z \gtrsim 0.5$) or X-ray luminosity (unconstrained AGN templates predict orders of magnitude higher X-ray luminosities, see also Figure 5). Instead, these additional fits suggest that an additional, possibly extended, dust distribution may be required. Similar modifications have been suggested for other SED templates in order to provide complete fits to other SMGs and millimetre-detected QSOs (e.g. Pope et al. 2008; Martínez-Sansigre et al. 2009; Rowan-Robinson et al. 2010). Unlike Rowan-Robinson et al. (2010), however, we find that a diffuse 'cirrus' component as described by Efstathiou & Rowan-Robinson (2003) is not sufficient for the additional dust distribution and does not improve the quality of our fits.

Table 6. Best-fit SED parameters using only the SB models. The SED derived X-ray luminosity is left as a free parameter and provides no additional constraint to the SED fitting. Errors are given at the 1σ confidence level after marginalizing over all other free parameters in the fitted templates. Col.(1): *Chandra* Source ID. Col.(2), (3), and (4): SB template normalization, age, and optical depth. Col.(5): Total model-derived, rest-frame bolometric IR luminosity from $\sim$0.001-1500μm. Col.(6): SFR derived from Eqn. 2 (§ 3.2.1) and Cols. 2 & 3. Col.(7): SED derived X-ray luminosity. Col.(8): Fractional contribution of model to observed 1.1mm flux. Col.(9): ln(L) of best-fit parameters.

Chandra ID	Norm	AGE Myr	τ_ν	IR Lum. $10^{12}L_\odot$	SFR $M_\odot$ yr^{-1}	X-ray Lum. 10^{43} ergs s^{-1}	f$_{1.1mm}$	ln(L)
(1)	(2)	(3)	(4)	(5)	(6)	(7)	(8)	(9)
J123616.08+621514.1	$7874.8^{+261.8}_{-247.1}$	$45.2^{+9.8}_{-6.9}$	$150.0^{+41.5}_{-41.5}$	$9.87^{+2.43}_{-2.47}$	822	$0.10^{+0.03}_{-0.03}$	1.22	-48.42
J123635.86+620707.8	$246.9^{+88.3}_{-81.7}$	$45.2^{+26.8}_{-12.9}$	$199.4^{+0.6}_{-88.3}$	$0.31^{+0.19}_{-0.19}$	26	$0.00^{+0.01}_{-0.01}$	0.04	-12.25
J123711.32+621331.1	$8412.4^{+156.2}_{-184.8}$	$56.9^{+6.1}_{-9.9}$	$199.0^{+1.0}_{-41.1}$	$7.41^{+2.63}_{-1.17}$	489	$0.08^{+0.03}_{-0.01}$	0.81	-28.15
J123711.98+621325.8	$2832.8^{+138.5}_{-625.4}$	$45.2^{+10.0}_{-7.0}$	$199.6^{+0.4}_{-48.2}$	$3.55^{+0.91}_{-0.92}$	296	$0.04^{+0.01}_{-0.01}$	0.30	-9.35
J123716.63+621733.4	$6318.3^{+67.8}_{-66.2}$	$36.8^{+6.9}_{-9.2}$	$200.0^{+0.0}_{-42.2}$	$10.30^{+3.30}_{-1.90}$	1003	$0.12^{+0.04}_{-0.03}$	1.14	-6057.59
J033158.25-274458.8	$1123.2^{+3.4}_{-2.3}$	$72.0^{+0.0}_{-6.9}$	$199.8^{+0.2}_{-43.2}$	$0.66^{+0.13}_{-0.01}$	31	$0.01^{+0.01}_{-0.01}$	0.29	-2217.17
J033204.48-274643.3	$302.8^{+57.6}_{-62.5}$	$71.9^{+0.1}_{-9.7}$	$101.1^{+86.4}_{-51.1}$	$0.18^{+0.06}_{-0.04}$	8	$0.00^{+0.01}_{-0.01}$	0.03	-26.34
J033207.12-275128.6	$253.3^{+14.9}_{-20.3}$	$71.8^{+0.2}_{-12.9}$	$198.9^{+1.1}_{-45.1}$	$0.15^{+0.06}_{-0.01}$	7	$0.00^{+0.01}_{-0.01}$	0.03	-23.76
J033209.71-274249.0	$2277.2^{+3.4}_{-3.4}$	$71.9^{+0.1}_{-6.8}$	$200.0^{+0.0}_{-43.2}$	$1.33^{+0.26}_{-0.01}$	63	$0.01^{+0.01}_{-0.01}$	0.72	-140057.35
J033212.23-274620.9	$2486.3^{+6.3}_{-6.7}$	$71.9^{+0.1}_{-6.8}$	$199.6^{+0.4}_{-42.2}$	$1.45^{+0.29}_{-0.01}$	68	$0.01^{+0.01}_{-0.01}$	0.36	-5567.86
J033215.32-275037.6	$3491.2^{+19.6}_{-20.2}$	$71.8^{+0.2}_{-6.8}$	$50.1^{+43.4}_{-0.1}$	$2.05^{+0.40}_{-0.02}$	96	$0.01^{+0.01}_{-0.01}$	0.42	-1261.17
J033222.17-274811.6	$2799.0^{+20.3}_{-21.8}$	$45.4^{+9.9}_{-7.2}$	$50.1^{+42.1}_{-0.1}$	$3.49^{+0.89}_{-0.88}$	289	$0.03^{+0.01}_{-0.01}$	0.49	-91.65
J033222.56-274815.0	$4147.3^{+24.7}_{-26.2}$	$72.0^{+0.0}_{-6.9}$	$50.7^{+42.5}_{-0.7}$	$2.42^{+0.49}_{-0.01}$	113	$0.02^{+0.01}_{-0.01}$	0.58	-69.91
J033235.18-275215.7	$109.1^{+4.3}_{-14.4}$	$57.0^{+6.2}_{-10.8}$	$198.8^{+1.2}_{-90.5}$	$0.10^{+0.04}_{-0.02}$	6	$0.00^{+0.01}_{-0.01}$	0.02	-328.50
J033238.01-274401.2	$1069.4^{+19.2}_{-17.5}$	$37.1^{+6.6}_{-9.5}$	$199.9^{+0.1}_{-43.0}$	$1.72^{+0.57}_{-0.32}$	167	$0.02^{+0.01}_{-0.01}$	0.21	-112.10
J033244.02-274635.9	$3419.4^{+38.9}_{-37.5}$	$45.2^{+9.9}_{-6.8}$	$101.1^{+40.9}_{-41.8}$	$4.29^{+1.03}_{-1.07}$	357	$0.04^{+0.01}_{-0.01}$	0.57	-101.89
J033246.83-275120.9	$917.1^{+6.7}_{-7.4}$	$71.8^{+0.2}_{-6.7}$	$199.9^{+0.1}_{-43.3}$	$0.54^{+0.10}_{-0.01}$	25	$0.01^{+0.01}_{-0.01}$	0.22	-4061.23
J033302.94-275146.9	$14138.5^{+225.5}_{-262.1}$	$37.0^{+6.6}_{-9.3}$	$99.6^{+42.0}_{-41.6}$	$22.80^{+7.40}_{-4.20}$	2223	$0.23^{+0.08}_{-0.05}$	2.56	-65.28
J095905.05+022156.4	$9410.8^{+175.9}_{-193.1}$	$45.1^{+9.9}_{-6.6}$	$150.7^{+41.5}_{-42.4}$	$11.80^{+2.80}_{-3.00}$	987	$0.13^{+0.03}_{-0.04}$	1.01	-4.61
J095929.70+021706.4	$5070.1^{+51.2}_{-211.0}$	$72.0^{+0.1}_{-13.7}$	$150.4^{+45.5}_{-47.6}$	$2.96^{+1.19}_{-0.02}$	139	$0.03^{+0.01}_{-0.01}$	0.44	-2.47
J095945.15+023021.1	$2282.0^{+10.1}_{-9.9}$	$71.9^{+0.1}_{-6.7}$	$100.1^{+41.6}_{-41.4}$	$1.34^{+0.26}_{-0.01}$	63	$0.01^{+0.01}_{-0.01}$	0.18	-706.44
J095953.85+021853.6	$1705.2^{+11.1}_{-10.2}$	$64.2^{+6.6}_{-6.1}$	$199.8^{+0.2}_{-42.7}$	$1.22^{+0.23}_{-0.19}$	69	$0.01^{+0.01}_{-0.01}$	0.15	-297.44
J095959.96+020633.1	$691.2^{+5.4}_{-5.3}$	$45.2^{+9.9}_{-7.1}$	$199.8^{+0.2}_{-42.7}$	$0.87^{+0.22}_{-0.22}$	72	$0.01^{+0.01}_{-0.01}$	0.08	-173.25
J100003.73+020206.4	$1049.4^{+31.6}_{-80.1}$	$71.9^{+0.1}_{-22.6}$	$50.3^{+42.8}_{-0.3}$	$0.62^{+0.50}_{-0.02}$	29	$0.00^{+0.01}_{-0.01}$	0.07	-21.81
J100006.11+015239.2	$3076.4^{+31.8}_{-82.1}$	$71.8^{+0.2}_{-13.1}$	$199.5^{+0.5}_{-45.4}$	$1.81^{+0.72}_{-0.03}$	85	$0.02^{+0.01}_{-0.01}$	0.24	-11.02
J100006.55+023259.3	$2005.4^{+13.9}_{-15.9}$	$72.0^{+0.1}_{-6.8}$	$199.9^{+0.1}_{-43.4}$	$1.17^{+0.23}_{-0.01}$	55	$0.01^{+0.01}_{-0.01}$	0.15	-4308.82
J100033.61+014902.0	$2553.0^{+30.1}_{-26.7}$	$71.9^{+0.1}_{-6.8}$	$200.0^{+0.1}_{-42.9}$	$1.49^{+0.29}_{-0.02}$	70	$0.02^{+0.01}_{-0.01}$	0.19	-327.48
J100055.34+023441.1	$20213.0^{+53.9}_{-59.2}$	$36.8^{+6.9}_{-9.0}$	$199.7^{+0.3}_{-41.9}$	$32.90^{+10.20}_{-6.20}$	3210	$0.38^{+0.12}_{-0.08}$	1.52	-10787.79
J100107.46+015718.1	$12755.5^{+126.0}_{-141.9}$	$26.1^{+9.2}_{-8.5}$	$199.6^{+0.4}_{-42.0}$	$28.40^{+7.10}_{-6.60}$	3459	$0.33^{+0.08}_{-0.08}$	1.48	-8393.19
J100116.15+023606.9	$6042.4^{+14.7}_{-16.6}$	$45.0^{+10.2}_{-6.7}$	$199.9^{+0.1}_{-42.6}$	$7.62^{+1.80}_{-1.97}$	637	$0.09^{+0.02}_{-0.02}$	0.61	-1990.78
J100139.73+022548.5	$70.0^{+0.5}_{-0.5}$	$71.9^{+0.1}_{-6.9}$	$198.9^{+1.1}_{-42.7}$	$0.04^{+0.01}_{-0.01}$	2	$0.00^{+0.01}_{-0.01}$	0.06	-189839.12

4 DISCUSSION

Across a $\sim$1.2 square degree area of the sky, we have analyzed the X-ray spectral and NIR-to-radio SED properties of 45 X-ray-detected AzTEC sources for evidence of AGN and starburst activity. Our full sample is limited by the number of available redshifts, leaving a subset (32/45) of sources. Within GOODS-N and GOODS-S, this subset of AzTEC/X-ray sources typically have high levels of dust obscuration ($N_H \gtrsim 10^{23}$ cm^{-2}) and are generally associated with AGN activity, while their NIR-to-radio SEDs imply that the IR and bolometric output are almost completely dominated by star formation. Though we do go deeper in the 4Ms GOODS-S field and find fainter potential X-ray counterparts, we do not find any evidence for significantly higher amounts of dust obscuration compared to the 2Ms GOODS-N and initial 2Ms GOODS-S. Considering the relative uncertainties in the L_X-SFR relation and under-prediction of the 1.1 mm flux for many of our models, a small portion ($\sim$6-13 percent) of our

X-ray-identified SMGs are likely to be completely dominated by starburst emission in both the X-ray and NIR-to-radio with the remaining majority powered almost exclusively by an AGN in the X-ray and starburst in the NIR-to-radio (see § 3.1.3 and § 3.2.2). Here, we explore the implications of our X-ray modeling and SED fitting in the context of emission at 1.1 mm and previous (sub-)mm/X-ray studies.

4.1 Origin of 1.1 mm Emission

As stated in § 3.2, (sub-)millimetre emission from our AzTEC/X-ray sources results from dust heated to T$\sim$30K. Based on our SED fitting (§ 3.2.2), the observed NIR-to-mm luminosity is generally dominated by the starburst with little contribution from an AGN (see Figure 3). These fits predict dust temperatures on the order of $\sim$30-40K yet generally under-predict the observed 1.1 mm flux by $\gtrsim$50 percent, suggesting that a cooler, extended dust component is present. Further evidence for an additional
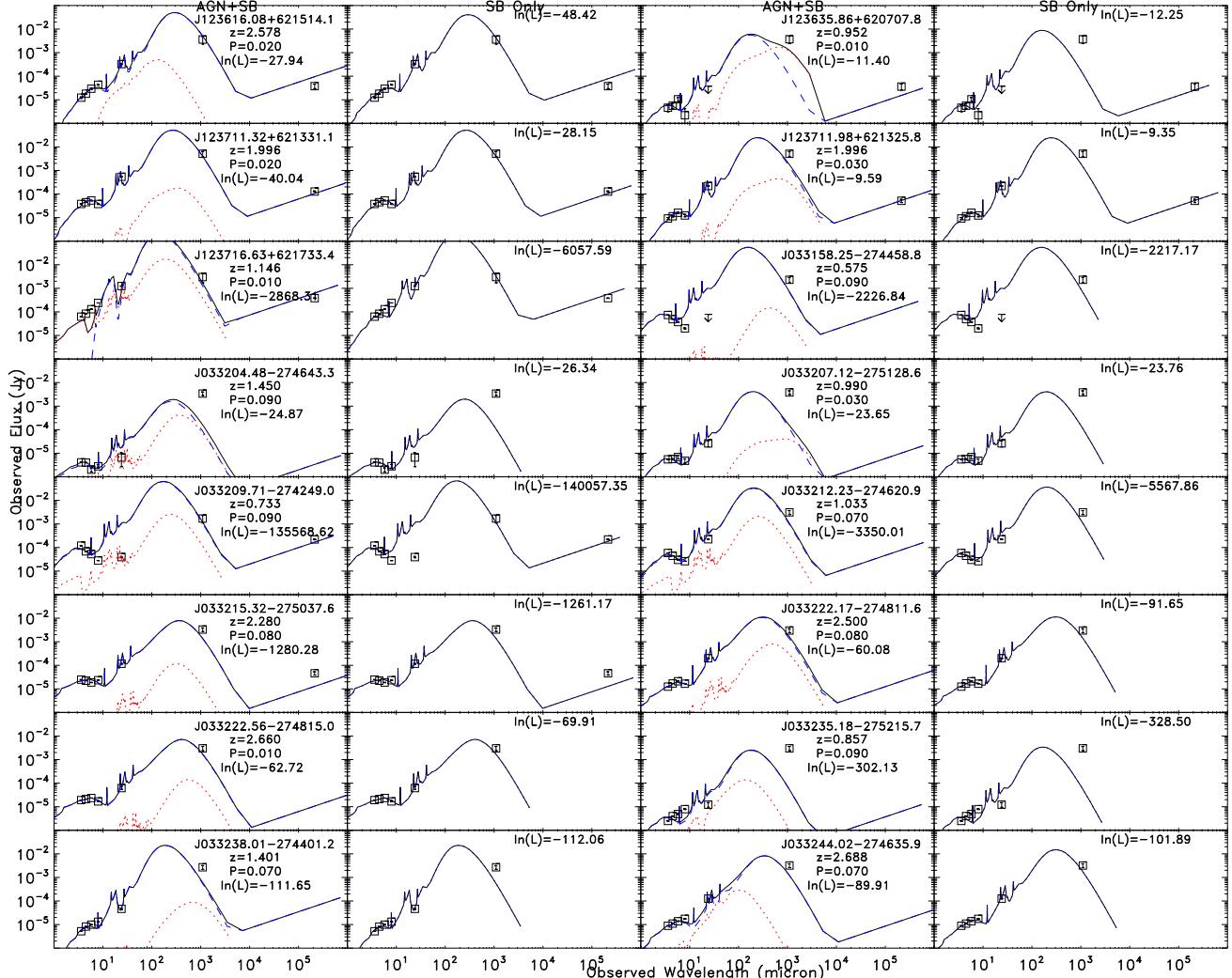
Figure 3. Observed frame best-fit AGN+SB and SB-only SEDs to AzTEC/X-ray sources. The plots show the template models that lie closest to the best-fit parameters determined from the MCMC SED fitting. The AGN and SB models are given by the dotted red and dashed blue lines, respectively, with their linear combination shown by the solid black line. Also shown for each source is the redshift used in the SED fitting, favoring the spectroscopic redshift where available, and the resulting best-fit ln(L) values. For reference, we have included the probability of random association P (Table 1) for each source.

dust component has been seen in previous SMG studies (e.g., Chapman et al. 2005; Pope et al. 2006) and by Rowan-Robinson et al. (2010) in *Herschel* SPIRE sources, although they suggest that it can be accounted for with the cirrus templates of Efstathiou & Rowan-Robinson (2003) which we are unable verify. Fitting of the IR dust peak, for which *Herschel* data are optimized, will provide more accurate estimates of the dust temperature and will aid in reducing parameter uncertainty, improving the bolometric luminosity estimates and providing further insight into the nature of the missing dust.

Given the evidence so far for an additional dust component, one must wonder where the dust resides. The dust could simply reside in an extended disk if the starbursting region remains localized to the central ∼1 kpc. Alternatively, the dust may reside in the halo of the SMG, pushed out through radiation- or momentum-driven outflows resulting from the starburst region(s) and/or the central AGN (e.g.,

Oppenheimer & Davé 2006; Zu et al. 2011). A typical GMC in a $z = 2$ starburst galaxy can reach velocities of ∼300 km s^{-1} (Murray, Ménard & Thompson 2011), which will spread its gas and dust as far as ∼15 kpc from the galaxy center during a ∼50 Myr starburst active phase. Similar outflows reaching ∼1000 km s^{-1} have been observed in local ULIRGS and have been shown to account for as much as 20 percent of the total molecular gas mass, on the order of 10^9 M$_\odot$, which are easily produced through starbursts with SFR$\gtrsim$ 100 M$_\odot$ yr^{-1} (Chung et al. 2009, 2011). The spatial scales predicted for these outflow regions are consistent with the radii predicted by the AGN templates and high resolution imaging of SMGs using the IRAM Plateau de Bure interferometer (PdBI) and Submillimetre Array (SMA) (e.g., Tacconi et al. 2006, 2008; Younger et al. 2008), which show typical size scales of ∼2-8 kpc. The molecular gas will not survive long due to lack of self-shielding, which would allow the dust to inhabit a larger volume than that traced by tra-
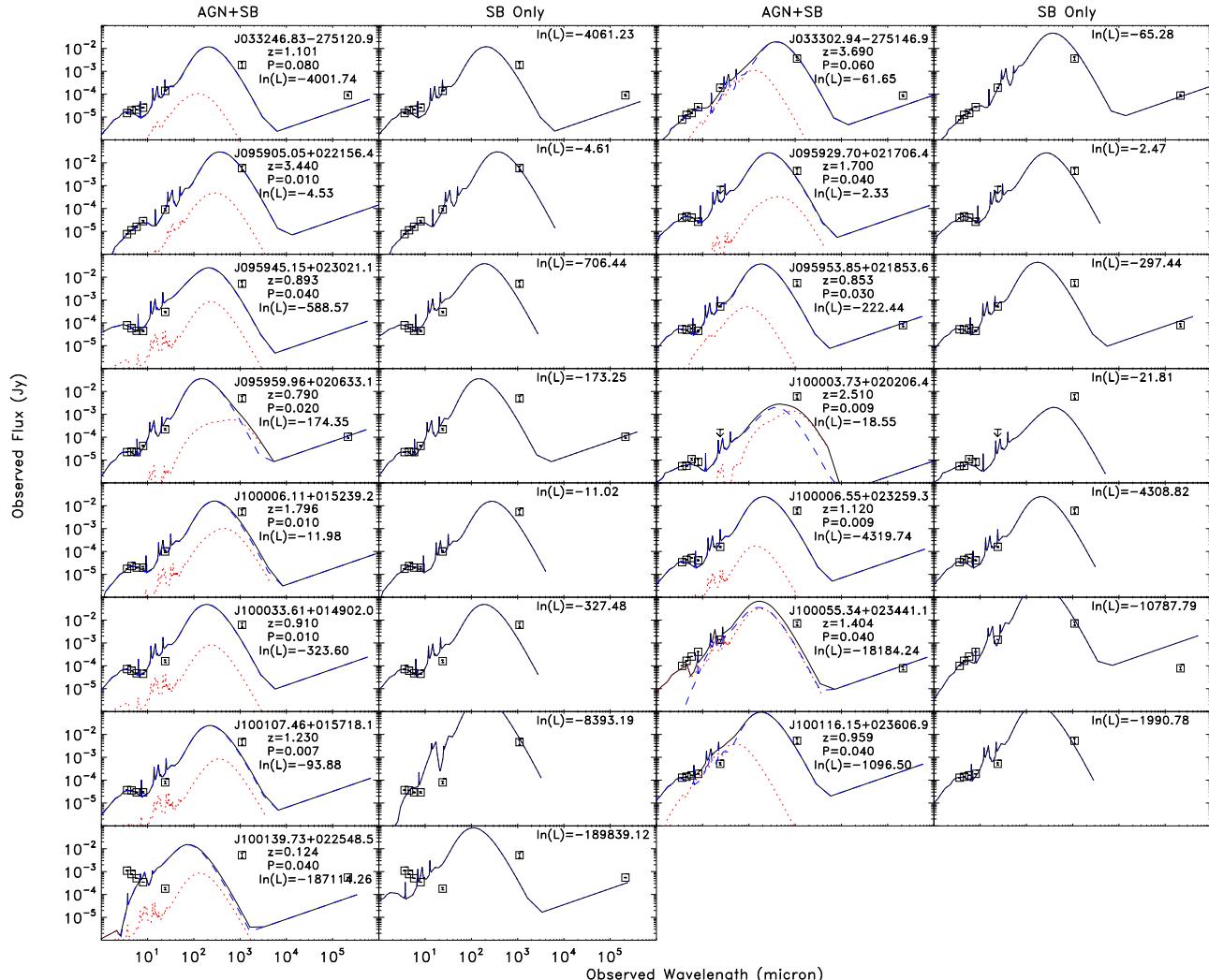
Figure 3 – *continued*

ditional molecular gas measurements. Though the majority of the mass will still be contained within the central region, the extended dust will quickly cool to the background temperature and will likely produce a temperature gradient as distance from the central region increases (see, for example, fig. 5 of Younger et al. 2008), which may contribute significantly to the (sub-)mm emission. This scenario agrees with the recent EVLA observations of Ivison et al. (2010, 2011) SMGs and of background quasars (Ménard et al. 2010).

A possible alternative to the extended cold dust model is that the missing 1.1 mm flux results from either false detections or source blending. We may readily remove false detections as the false association rate for the X-ray-identified AzTEC sources is ∼5-6 percent (§ 2.3.1) whereas the majority of sources under-predict the 1.1 mm flux. Similarly, previous sub-mm studies suggest blending can occur in ∼20-25 percent of sub-mm detected sources (see Scott et al. 2012, and references therein) so that while blending is likely to occur, it is unlikely to the primary cause for the flux discrepancy. Unfortunately, it is not possible to de-blend sources using current *Spitzer* MIPS, *Herschel* PACS or

VLA radio data without *a priori* knowledge of the intrinsic sources. Only through high resolution imaging and kinematics with ALMA, LMT and future (sub-)mm telescopes may we be able to de-blend potential offenders and/or make direct confirmation of an outflow-produced, extended cold dust distribution.

The question still remaining is how the AGN emission, as indicated by the high X-ray detection rate and the X-ray spectra, relates to the sub-mm observations. While AGN models are favored in the X-ray spectral fitting, the sub-mm emission is, in fact, unlikely to result solely from an AGN. As shown in Figure 5, the X-ray priors prevent any significant contribution from the AGN templates. Even when relaxed, the AGN models still show poor fits to the mid-IR, relative to their observed fluxes and uncertainties, and sub-mm data, never mind the unphysical X-ray luminosity predicted. In a merger-driven formation scenario (e.g. Narayanan et al. 2010), gas from the colliding systems gives rise to an increase in star formation, resulting in a sub-mm-bright phase. Shortly after the sub-mm-bright phase and final coalescence, the central black hole may undergo the
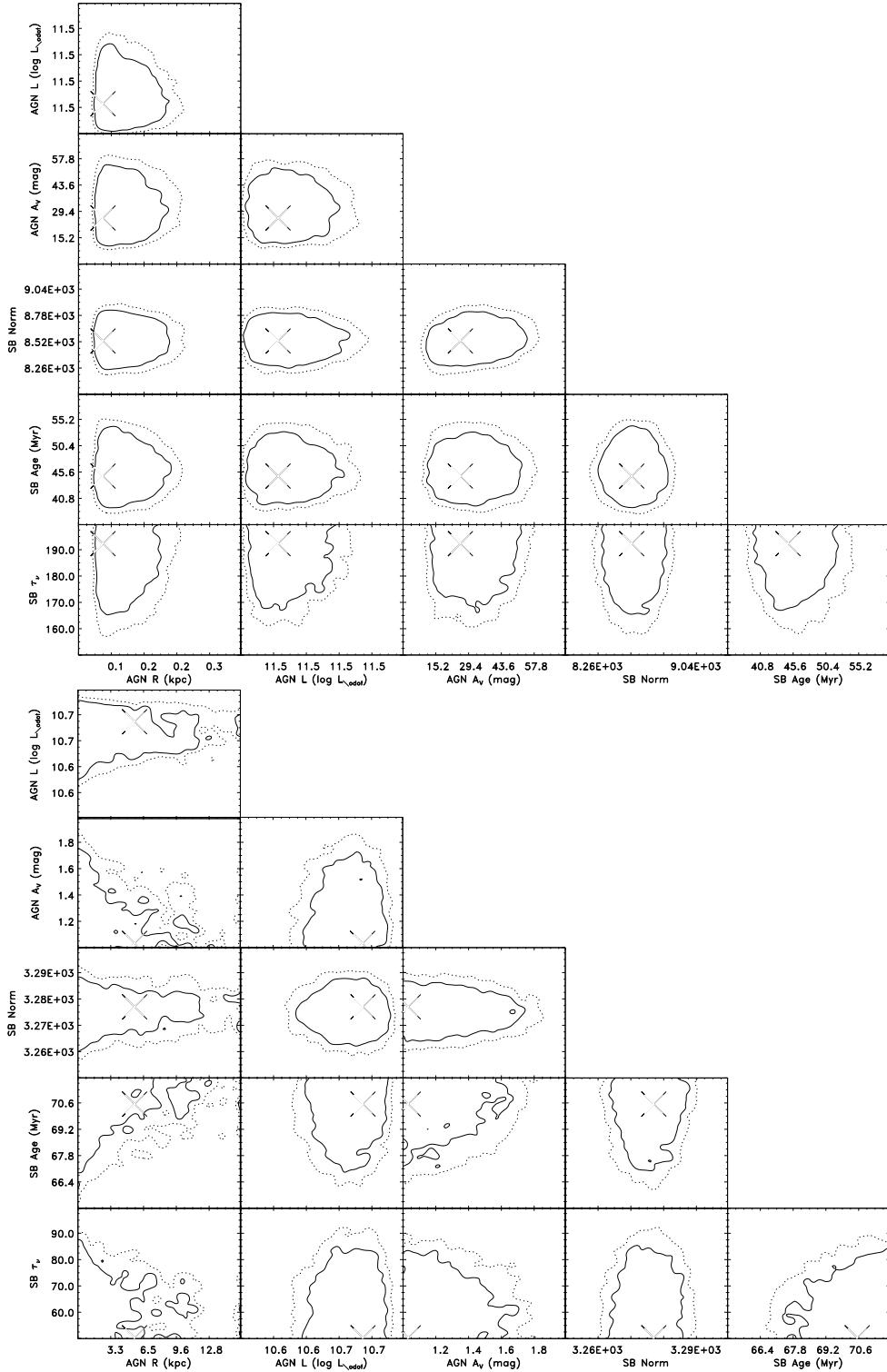
Figure 4. Smoothed, marginalized likelihood distribution of accepted parameter steps for J123616.08+621514.1 (top) and J033215.32-275037.6 (bottom), using the AGN+SB templates. A description of each parameter in the AGN and SB templates is given in § 3.2.1. The location of the maximum likelihood value has been marked by the large 'X'. Contours are drawn at the 68 percent (solid) and 90 percent (dashed) confidence levels. The likelihood distributions show that while there are no large apparent correlations between parameters, the constraints on some parameters are rather poor (particularly for AGN R and SB τ_ν). AGN L and SB normalization are the most well constrained due to the inclusion of the X-ray luminosity prior.
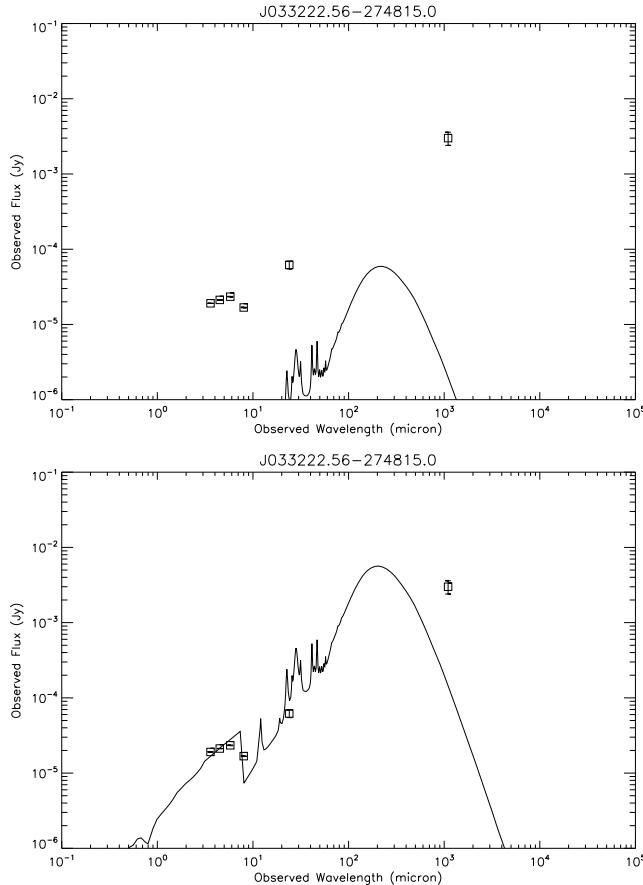
Figure 5. AGN only fits for J03222.56-274815.0 using the X-ray priors (top) and without (bottom). As seen in Figure 3, the AGN component is unable to contribute any more to the NIR-to-radio SED as its vertical scaling, i.e. luminosity, is set by the X-ray priors. Without these constraints, the models are able to account for some of the mid-IR emission, still missing the bulk of the sub-mm flux, but would predict tremendous X-ray luminosities; here the best fit AGN L is $\sim 10^{12.75}$ $L_\odot$ which translates to an X-ray luminosity of $\sim 5.9 \times 10^{44}$ ergs s^{-1}, many times over what is actually observed.

Figure 6. Histogram of effective power-law indexes ($\Gamma_{\rm Eff}$) for the AzTEC/X-ray sources, given by the filled histogram, for all sources (top) and only those with radio counterparts (bottom). For comparison, we also include the $\Gamma_{\rm Eff}$ distributions from A05b (back-hashed region) and LNPS10 (forward-hashed region).

bulk of its growth, producing an AGN which may then aid in shutting off the star formation through feedback, leaving the final system as a quasar or dusty AGN-powered ULIRG. Given the high X-ray column densities we derived for our AzTEC/X-ray sample, it is likely that these sources represent the early growth phase of the AGN. Combined with the starburst-dominated NIR-to-radio SEDs and expected short timescale of the sub-mm-bright phase (< 50 Myr), the X-ray-identified sources may be SMGs caught in their transitionary period between peak star formation and peak black hole growth. This transition scenario is consistent with the fact that the average 1.1 mm fluxes and 2-10 keV count rates of the X-ray-identified sources are both below the average of the overall SMG and X-ray sample. The remaining X-ray undetected SMGs could result from a starburst triggered during the first passing of merging systems or rapid, short-lived mergers similar to those found by Chapman et al. (2009). However, we can not rule out the possibility that the X-ray-dim SMGs could result from a moderately continuous gas in-fall (see, for example, Davé et al. 2010) or very young

starbursts with Compton-thick AGNs (e.g., A05a,b). The X-ray-detected SMGs are unlikely to be produced by such continuous in-fall given the starburst timescales from our SED modeling; accretion-driven models predict that the sub-mm bright phase may last for $\sim$0.1-1 Gyr (Fardal et al. 2001). One other possibility given the expected high SFRs for SMGs is that the central AGN are likely time-variable (see Alexander & Hickox 2012, and references therein). AGN can switch between being 'on' or 'off' on timescales of $\lesssim 1$ yr and cause large variations in their observed luminosities and absorbing column densities, which will affect the probability of detecting an AGN associated with an SMG. It is unknown how this AGN time-variability scenario will influence the SED of SMGs though we expect any contribution to be small given the already low AGN contribution rate. Further evolutionary simulations and observations aimed at spatially resolving SMGs will provide the tools necessary to classify SMGs under the appropriate formation and evolutionary scenario.
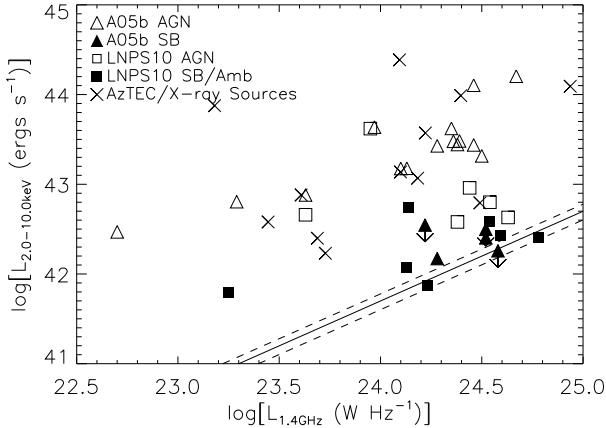
Figure 7. Reproduction of fig. 2b from A05b including the A05b, LNPS10 and AzTEC/X-ray samples. The fluxes of A05b have been converted to 2.0-10.0 keV luminosities assuming a photon index of $\Gamma = 1.8$ and eqn. 1 of Alexander et al. (2003). Radio luminosities are calculated from the radio fluxes in Table 2 and eqn 2. of Alexander et al. (2003). Also plotted is the P04 SFR-X-ray luminosity relation (solid line), using the SFR-radio relation of Condon (1992) to convert SFR to 1.4 GHz luminosity, with a 20 percent statistical error given by the dotted lines. Some of the A05b starburst sources only have 3σ upper limits for their X-ray luminosities and are shown with arrows indicating such.


Figure 8. Reproduction of fig. 8 from A05b including the A05b, LNPS10 and AzTEC/X-ray samples. The X-ray fluxes of A05b are converted to 2.0-10.0 keV using $\Gamma = 1.8$. FIR luminosities are derived from the radio luminosities of Fig. 7 using a radio to FIR correlation of q=2.35 (Helou, Soifer & Rowan-Robinson 1985). The over-plotted lines represent ratios of constant X-ray versus FIR luminosity for the A05b starburst ($\frac{L_X}{L_{FIR}} = 10^{-4}$) and AGN ($\frac{L_X}{L_{FIR}}$=0.004) sources, and the average luminosity ratio for quasars studied by Elvis et al. (1994) ($\frac{L_X}{L_{FIR}}$=0.05).

4.2 Comparison with Previous Studies

For our AzTEC/X-ray sample, the AGN detection rate is ∼14 percent between all three fields. However, the shallow X-ray depth of COSMOS, potentially compounded by our more stringent detection criteria, prevents confirmation of the most heavily obscured AGNs which may contribute significantly to the sub-mm emission (Lutz et al. 2010; Hill & Shanks 2011). Excluding COSMOS, the AGN detection rate increases to ∼ 28 percent, consistent with previous X-ray/SMG studies ($> 38^{+12}_{-10}$ percent, 29±8 percent and $< 26 \pm 9$ for A05a,b, LNPS10 and GRC11, respectively) while avoiding potential biases due to prior counterpart identification and achieving better source statistics via larger sky coverage. Similar to LNPS10, we also find evidence that ∼6-13 percent of our X-ray sources are potentially HMXBs associated with high star formation rates. However, many of the starburst powered SCUBA-detected sources of LNPS10, and by extension A05b, are missing from our sample. While the our X-ray data for GOODS-N is essentially the same as that used in A05b and LNPS10, it is not surprising for differences to exist between the AzTEC and SCUBA catalogs. Chapin et al. (2009) suggests that such a discrepancy results from instrument and measurement calibration uncertainty as well as intrinsic spread in host properties (namely dust temperature and emissivity). In fact, for a SCUBA source to be detected by AzTEC at $> 3.5\sigma$ in GOODS-N (where the AzTEC rms is ∼1.3 mJy/beam, see § 2.1), its effective $850\mu m$ flux would need to be $\gtrsim 8.19$ mJy, higher than the typical $850\mu m$ flux for sources in LNPS10. This estimate assumes an R=$S_{850}/S_{1.1}$ value of 1.8 (Chapin et al. 2009) and that 'flux boosting' (see, for example, Austermann et al. 2010; Scott et al. 2010) effects the

$850\mu m$ and 1.1mm observations equally. Completeness of the (sub-)mm observations may also contribute to this discrepancy; at ∼4mJy, the AzTEC map is ∼60 percent complete (Perera et al. 2008). Of course, there is always the issue of false identifications and mismatching of sources as well as prior counterpart bias (see LNPS10) which, while the expected number of such occurrences are small (see § 2), may still lead to a decrease in the number of starburst-dominated X-ray sources in our sample.

In Figure 6, we show the range of effective photon indexes Γ_{Eff} for our AzTEC/X-ray sample (see § 3.1.1, Table 3) in relation to the samples of A05b and LNPS10. Using the Mann-Whitney (MW) U-test, we find that the probability that our AzTEC/X-ray sources are consistent with being drawn from the samples of A05b and LNPS10 are 0.02 and 0.14, respectively. If we limit our sample to AzTEC/X-ray sources with radio detections then the MW probabilities become 0.07 and 0.17 for the A05b and LNPS10 samples, respectively. Since the errors on Γ_{Eff} are known, we further estimate the intrinsic mean and variance of the samples by constructing 1000 Monte Carlo realizations of the Γ_{Eff} distributions. The resulting intrinsic mean value of Γ_{Eff} for the AzTEC/X-ray, A05b and LNPS10 samples are 1.14±0.09 (1σ), 0.60±0.10 and 1.44±0.16, respectively; including only the radio-detected AzTEC/X-ray sources results in an intrinsic mean of 1.05±0.08. These results imply a strong statistical difference between the AzTEC/X-ray and A05b samples (at $\gtrsim 3\sigma$), while the AzTEC/X-ray and LNPS10 samples have consistent means values of Γ_{Eff}.

Despite the differences in Γ_{Eff}, the methods of analysis in A05b produce results consistent with our study. For further comparison, we reproduce figures 2b and 8 of A05b, which show the $L_{2.0-10.0keV}$ versus $L_{1.4GHz}$ (Figure 7) and $L_{2.0-10.0keV}$ versus L_{FIR} (Figure 8) relations for the A05b

and LNPS10 starburst and AGN systems, including our AzTEC/X-ray sources that have radio counterparts. In reproducing the A05b figures, we have converted the A05b 0.5-8.0 keV fluxes to 2.0-10.0 keV luminosities assuming a photon index of $\Gamma = 1.8$ and eqn. 1 of Alexander et al. (2003). Radio and FIR luminosities have been determined for our sample following the same procedures as A05b to ensure compatibility. We caution, however, that the radio-FIR correlation used to derive the FIR luminosities from the radio emission (Helou, Soifer & Rowan-Robinson 1985) assumes emission purely from star formation and could be misleading if the AGN is radio-loud (e.g. Donley et al. 2005, 2010). Figures 7 and 8 show that the X-ray emission for the sub-sample of radio-identified AzTEC/X-ray sources is higher than one would predict from their radio and/or FIR luminosities if they resulted purely from star formation, indicating AGN activity. However, the FIR luminosities are generally higher than expected for typical quasars which suggests significant contribution from star formation, again consistent with the results from § 3.2. Alternatively, sources could lie above the Elvis et al. (1994) quasar relation if they are reflection dominated or Compton-thick (e.g. FSC 10214+4727 A05b, Arp 220 Iwasawa et al. 2005). This is not likely to affect our analysis based on the results from our X-ray spectral modeling (§ 3.1); nevertheless, we can not rule out the possibility that the faintest X-ray sources may be harboring highly luminous, Compton thick AGNs, particularly for the non-X-ray-detected SMGs (e.g. Iwasawa et al. 2005; Lutz et al. 2010; Hill & Shanks 2011).

4.3 Cross-Correlation of AzTEC/X-ray source populations

In addition to examining X-ray-detected SMGs on a source-by-source basis, a simple cross-correlation analysis of the X-ray and AzTEC source populations can identify evolutionary patterns between the populations. Almaini (2002); Almaini et al. (2003) were the first to measure the angular cross-correlation function (XCF) between SMGs and X-ray sources and found significant correlation at large scales, leading to the conclusion that the populations both reside in similarly massive dark matter halos and trace the same large scale structure. Hill & Shanks (2011) later estimated the XCF for LABOCA sources in the ECDFS and while found similar evidence for small scale clustering, i.e. residing in same dark matter halos, found no evidence for large scale clustering, consistent with Borys et al. (2004). Roche, Dunlop & Almaini (2003) measured the XCF of extremely red objects (EROs) – which may be the signature of massive galaxies that have entered their passive post-AGN phase in galaxy evolution – and X-ray sources in the CDFS, and again find evidence for significant correlation. Together, these results may suggest an evolutionary sequence between these three populations, where starburst dominated SMGs go through an AGN-bright phase before evolving into passive ellipticals or EROs.

To determine if there is any correlation between the AzTEC and *Chandra* source populations, we apply the two-point angular XCF, $w_{AX}(\theta)$, defined as the excess probability of finding both an AzTEC source in a solid angle $\delta\Omega_A$ and an X-ray source in a solid angle $\delta\Omega_X$, with an angular separation θ from each other. This excess proba-
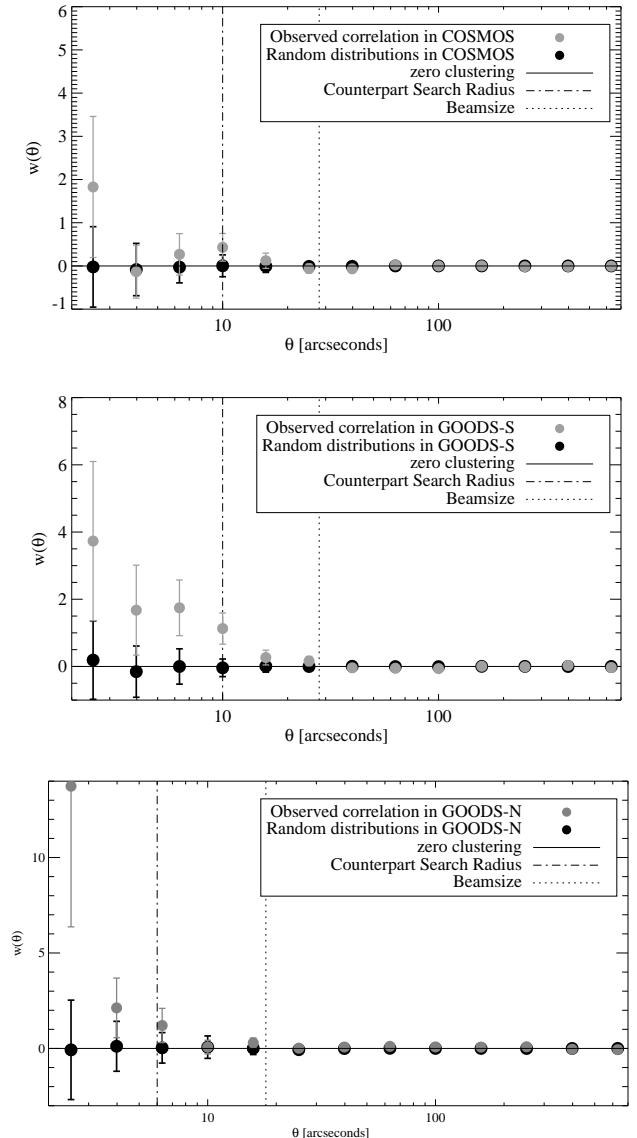

Figure 9. The XCF between AzTEC and *Chandra* source populations. Plotted in each panel is the observed XCF and the XCF from randomly generated source populations along with the respective beam-size and search radius for each field. Below our adopted search radii, the XCF shows significant signal due to detected counterparts. The lack of consistent positive correlation in COSMOS results from the shallow X-ray depth and corresponding low source density.

bility (relative to an uncorrelated distribution) is given by $\delta P = \rho_A \rho_X [1 + w_{AX}(\theta)] \delta\Omega_A \delta\Omega_X$, where ρ_A and ρ_X are the surface densities of AzTEC and X-ray galaxies on the sky (Peebles 1980). In practice this can be measured from galaxy maps by counting the number of SMG/X-ray source pairs, binned by their angular separation, and comparing to pair counts from random positions. Here, we use the cross-correlation adaptation to the Landy-Szalay estimator (Landy & Szalay 1993), which is given by

$$w_{AX}(\theta) = \frac{D_A D_X(\theta) - D_A R_X(\theta) - D_X R_A(\theta) + R_A R_X(\theta)}{R_A R_X(\theta)}$$

$$(3)$$
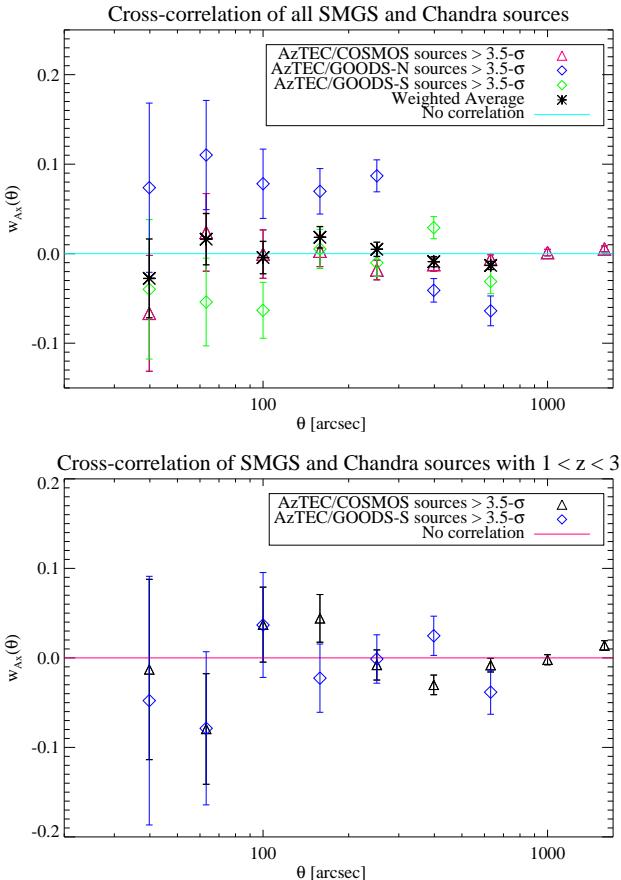
Figure 10. The XCF between the AzTEC and *Chandra* source populations (shown in Figure 9) at scales larger than the beam-size. The top panel shows the full sample while the bottom shows the XCF in the redshift range 1< z <3. Over the three fields, there is no significant correlation between the source populations, particularly over the typical redshift range of SMGs. Due to sensitivity variations in the *Chandra* data, the XCF should not be heavily weighed at angular separations of ≳200.

where $D_A D_X$ is the number of SMG/X-ray source pairs, $D_A R_X$ and $D_X R_A$ are the number of pairs found between each galaxy catalog and randomly generated positions of sources within each angular separation bin. $R_A R_X$ is the number of pairs found between random positions for each galaxy population, generated from the selection function and sensitivity distribution of each map. To generate random source distributions for the AzTEC maps, we follow the methods of Williams et al. (2011). For the *Chandra* random catalogs, the exposure maps are relatively uniform (ignoring effects due to CCD gaps and edge overlapping in COSMOS as they are generally small) such that we may produce the random catalogs by simply randomly generating positions within the overlapping coverage region of the *Chandra* and AzTEC maps. Note, however, that this does not take into account the sensitivity variations (mostly due to PSF degradation) as a function of off-axis distance; the XCF may thus be incorrect at scales larger than ~200″. The overlapping observations in COSMOS helps to smooth the telescope response, allowing for a more accurate XCF at larger scales.

The resulting XCF for each field, as well as the ex-

pected XCF from completely random distributions, is shown in Figure 9, where the errors are estimated from a Poissonian distribution given the number of AzTEC/X-ray pairs in each angular bin. The expectation from random distributions is estimated by averaging the XCF of 100 AzTEC and X-ray random distributions described above, which have the same properties (area and source density) as the observed maps. In the case of the random expectation, the errors correspond to the standard deviation of the XCF from each of the individual random distributions. At small scales, there is significant positive correlation in the observed XCF due to identified counterparts (see also Hill & Shanks 2011); this effect is diluted in COSMOS due to its shallow X-ray depth and thus low source density compared to either GOODS field. However, since the AzTEC source positions are not well known on scales smaller than the beam-size, we choose to limit our XCF analysis to the large scale clustering. Figure 10 shows the same XCF combined with their weighted average for scales larger than 28″, the beam-size of AzTEC on ASTE, though we caution against heavy interpretation at scales larger than ~200″ as previously mentioned.

Across the three fields, we find no evidence for any large scale correlation signal; any apparent correlation or anti-correlation seen in individual fields is detected at ≲ 1σ confidence, consistent with Borys et al. (2004) and Hill & Shanks (2011). The large area covered by our sample (~1.2 square degrees) aids in mitigating the effects of cosmic variance, which is the likely cause of variation between fields and may affect the positive correlation signal found in Almaini (2002). It is possible that the lack of any correlation signal in our data may be the result of dilution given the wide and differing redshift distributions of the X-ray and sub-mm sources. In an attempt to improve the cross-correlation signal, we have run the same analysis by limiting the X-ray sources to the redshift range of $1 < z < 3$ where the X-ray redshift distribution shows significant overlap with the sub-mm distribution. If there is any cross-correlation between the two samples, it should be maximized here. Due to the small number of X-ray sources with available redshifts in GOODS-N (49 out of the original 397), we excluded this field from the XCF in the 1< z <3 redshift range. The XCF using this redshift-limited subset for GOODS-S and COSMOS is statistically identical to the result we measured using the entire set of X-ray sources, i.e. no evidence for a correlation.

The lack of a significant correlation between the X-ray and AzTEC source populations at large scales may suggest that SMGs and AGN are not universally related in terms of dark matter halo mass and large scale structure. However, considering the significant fraction of AzTEC SMGs that do have plausible X-ray detections here, it is likely that the SMG phenomenon is not governed by a single formation and evolution process; rather, the SMG population is a "mixed bag" of systems – some undergoing major mergers concurrent with the build-up of massive black holes (e.g., Narayanan et al. 2010) and others signaling a short-lived phase of intense star-formation in more normal galaxies (e.g., Chapman et al. 2009) or even quiescent mass build-up from gas in-fall (e.g., Davé et al. 2010) (see also § 4.1). Such cases are likely tied to the host's intrinsic properties which could naturally explain the enhanced sub-mm emission from bright, obscured AGNs as found by Lutz et al. (2010) and Hill & Shanks (2011). However, we caution that limitations

in measuring the correlation between these populations can also give a null result. For example, the large volume sampled coupled with the lack of redshift information for the full X-ray and SMG catalogs will necessarily dilute the *projected* correlation strength between the two populations, even if there is some spatial correlation. The shallow X-ray depth of COSMOS will further dilute any correlation signal by primarily detecting bright AGN that are likely well past their starburst phase. Observations of SMGs in the near-future with ALMA and the LMT geared towards measuring their redshifts and obtaining high-resolution imaging of their dust and gas will greatly aid in the development and fine tuning of formation and evolution scenarios for this population.

5 SUMMARY

We have presented a detailed analysis of the X-ray properties of AzTEC 1.1 mm sources found in the GOODS-N, GOODS-S and COSMOS fields. Thanks to deep ($\sim$2-4 Ms) *Chandra* observations, we find X-ray counterparts to $\sim$14 percent of the 1.1 mm sources across all three fields, increasing to $\sim$28 percent if we exclude COSMOS due to its shallower X-ray data. From our modeling of the X-ray spectra and NIR-to-radio SEDs, we conclude that AzTEC/X-ray sources are all starburst-dominated in the IR, with SFRs on the order of $100-1000$ $M_\odot yr^{-1}$, whereas an AGN component is needed in order to explain the observed X-ray luminosities for the majority of our sources. In $\sim$6-13 percent of our sample, we find evidence for X-ray emission consistent with high SFRs, after accounting for the relative uncertainties in the L_X-SFR relations and the typical under-prediction of the 1.1 mm flux in our SED modeling. The AGNs typically appear obscured in the X-ray band, with neutral hydrogen column densities in excess of 10^{23} cm^{-2}. These results are consistent with other SMG/X-ray studies. Overall, the AGN templates contribute very little ($\lesssim$10 percent) to both the bolometric luminosity and 1.1mm flux. At 1.1 mm in particular, the AGN+SB models typically under-predict the observed fluxes, which indicates that either a cooler, extended dust component is required to fully recover the NIR-to-radio SED or that the sources are blended. We suggest that this missing dust could result from radiation- and/or momentum-driven outflows caused by the starburst/AGN regions, which pushes the dust out into the halo where it cools rapidly and, although it accounts for a small fraction of the total dust mass, may contribute significantly to the 1.1 mm emission.

The high AGN identification rate in these AzTEC SMGs is particularly interesting in regards to SMG formation and evolution scenarios. Following a merger-driven scenario, the X-ray identified sources could represent the transitional period between starburst and AGN dominant phases. However, the lack of a significant correlation at large scales between all X-ray sources and SMGs in these fields suggests that not all SMGs will evolve to possess an AGN and, similarly, that not all AGN evolve from a sub-mm bright phase. This suggests heterogeneity in the formation/evolution of SMGs, possibly due to either intrinsic source properties, i.e. amount of obscuration, or even multiple formation scenarios. With future analyses aimed at source evolution as a function of redshift, combined with a more comprehensive redshift catalog for SMGs (one of the goals for the upcoming LMT), we will be able to determine the AGN fraction and contribution to greater certainty, allowing for investigating how SMGs form and evolve into the galaxies we see in the local Universe.

REFERENCES

Alexander D.M. et al. 2003, AJ, 126, 539

Alexander D.M., Smail I., Bauer F.E., Chapman S.C., Blain A.W., Brandt W.N., Ivison R.J. 2005, Nature, 434, 738

Alexander D.M., Bauer F.E., Chapman S.C., Smail I., Blain A.W., Brandt W.N., Ivison R.J. 2005, ApJ, 632, 736

Alexander D.M., Hickox R.C. 2012, New Astronomy Reviews, 46, 93

Almaini O. 2002, A New Era in Cosmology, eds. Metcalfe N. & Shanks T., ASP Conf. Series, 283, 377

Almaini O. et al. 2003, MNRAS, 338, 303A

Alonso-Herrero A. et al. 2011, ApJ, 736,82

Aretxaga I., Wilson G.W., Aguilar E., Alberts S., Scott K.S., Scoville N., Yun M.S., Austermann J., Downes T.P., Ezawa H., Hatsukade B., Hughes D.H., Kawabe R., Kohno K., Oshima T., Perera T.A., Tamura Y., Zeballos M. 2011, MNRAS, 415, 3831A

Arnaud K.A. 1996, Astronomical Data Analysis Software and Systems V., eds. Jacoby G. & Barnes J., ASP Conf. Series, 101, 17

Arnaud K.A. 2003, ApJ submitted

Austermann J.E. et al. 2010, MNRAS, 401, 160

Barger A.J., Cowie L.L., Sanders D.B., Fulton E., Taniguchi Y., Sato Y., Kawara K., Okuda H. 1998, Nature, 394, 248

Barger A.J. et al. 2003, AJ, 126, 632

Barger A.J., Cowie L.L., Wang W.-H. 2008, ApJ, 689, 687

Bielby R.M., Hill M.D., Metcalfe N., Shanks T. 2012, MNRAS, 419, 1315

Bertoldi F. et al. 2007, ApJS, 172, 132

Blain A.W., Smail I., Ivison R.J., Kneib J.-P., Frayer D.T. 2002, Physics Reports, 369, 111

Blain A.W., Chapman S.C., Smail I., Ivison R. 2004, ApJ, 611, 52

Borys C., Scott D., Chapman S., Halpern M., Nandra K., Pope A. 2004, MNRAS, 355, 485

Carilli C.L., Yun M.S. 2000, ApJ, 530, 618

Cash W. 1979, ApJ, 228, 939

Chapman S.C., Blain A.W., Smail I., Ivison R.J. 2005, ApJ, 622, 772

Chapman S.C., Blain A.W., Ibata R., Ivison R.J., Smail I., Morrison G. 2009, ApJ, 691, 560

Chapin E.L. et al. 2009, MNRAS, 398, 1793

Chung A., Narayanan G., Yun M.S., Heyer M., Erickson N.R. 2009, ApJ, 138, 858

Chung A., Yun M.S., Narayanan G., Heyer M., Erickson N. R. 2011, ApJL accepted, arXiv:1103.5508v1

Condon J.J., Anderson M.L., Helou G. 1991a, ApJ, 376, 95

Condon J.J. 1992, ARAA, 30, 575

Coppin K.E. et al. 2006, MNRAS, 372, 1621

Coppin K.E. et al. 2008, MNRAS, 389, 45C

Davé R., Finlator K., Oppenheimer B.D., Fardal M., Katz N., Keres D., Weinberg D.H. 2010, MNRAS, 404, 1355

de Zotti G., Massardi M., Negrello M., Wall J. 2010, A&ARv, 18, 1

Dicken D. et al. 2012, ApJ, 745, 172

Donley J.L., Rieke G.H., Rigby J.R. Pérez-González P.G. 2005, ApJ, 634, 169

Donley J.L., Rieke G.H., Alexander D.M., Egami E., Pérez-González P. G. 2010, ApJ, 719, 1393

Downes A.J., Peacock J.A., Savage A., Carrie D.R. 1986, MNRAS, 218, 31

Downes T.P. et al. 2011, MNRAS submitted, arXiv:1103.3072

Efstathiou A., Rowan-Robinson M., Siebenmorgen R. 2000, MNRAS, 313, 734

Efstathiou A., Rowan-Robinson M. 2003, MNRAS, 343, 322

Elvis M et al. 1994, ApJS, 95, 1

Elvis M et al. 2009, ApJS, 184, 158E

Ezawa H. 2008, SPIE, 7012E, 6

Fardal M., Katz N., Weinberg D.H., Davé R., Hernquist L. 2001, ApJ submitted, arXiv:astro-ph/0107290v1

Ferrarese F., Merritt D. 2000, ApJ, 539, 9

Fritz J., Franceschini A., Hatziminaoglou E. 2006, MNRAS, 266, 767

Gebhardt K. et al. 2000, ApJ, 539, 13

Gelman A., Roberts G.O., Gilks W.R. 1996, Bayesian Statistics 5, eds. Bernado J.M, Berger J., Dawid A.P., Smith A.F.M, Oxford: Oxford University Press

Georgantopoulos I., Rovilos E., Comastri A. 2011, A&A, 526, A46

Granato G.L. & Danese L. 1994, MNRAS, 268, 235

Grimm H.-J., Gilfanov M., Sunyaev R. 2003, MNRAS, 339, 793

Gultekin et al. 2009, ApJ, 698, 198

Helou G., Soifer B.T., Rowan-Robinson M. 1985, ApJ, 298, 7

Heywood I., Bielby R.M., Hill M.D., Metcalfe N., Rawlings S., Shanks T., Smirnov O.M. 2012, MNRAS accepted, arXiv:1209.4660

Hill M.D. & Shanks T. 2011, MNRAS, 410, 762

Hopkins P.F, Younger J.D., Hayward C.C., Narayanan D., Hernquist L. 2010, MNRAS, 402, 1693

Holland W.S. et al. 1999, MNRAS, 303, 659

Hughes D.H. et al. 1998, Nature, 394, 241

Ivison R.J. et al. 2005, MNRAS, 364, 1025

Ivison R.J. et al. 2007, MNRAS, 380, 199

Ivison R.J., Smail I., Papadopoulos P.P., Wold I., Richard J., Swinbank A.M., Kneib J.-P., Owen F.N. 2010, MNRAS, 404, 198

Ivison R.J., Papadopoulos P.P., Smail I., Greve T.R., Thomson A.P., Xilouris E.M., Chapman S.C. 2011, MNRAS, 412, 1913

Iwasawa K., Sanders D.B., Evans A.S., Trentham N., Miniutti G., Spoon H.W.W. 2005, MNRAS, 357, 565

Kellermann K. I., Fomalont E. B., Mainieri V., Padovani P., Rosati P., Shaver P., Tozzi P., Miller N., 2008, ApJS, 179, 71

Kennicutt R.C. 1998, ARAA, 36, 189

Laird E.S., Nandra K., Pope A., Scott D. 2010, MNRAS, 401, 2763

Landy S.D., Szalay A.S. 1993, ApJ, 412, 64

Le Floc'h E. et al. 2005, ApJ, 632, 169

Lucy L.B. 2000, MNRAS, 318, 92

Luo B. et al. 2008, ApJS, 179, 19

Lutz D. et al. 2010, ApJ, 712, 1287

Magdziarz P., Zdziarski A.A. 1995, MNRAS, 273, 837

Marconi A., Risaliti G., Gilli R., Hunt L.K., Maiolino R., Salvati M. 2004, MNRAS, 351, 169

Martínez-Sansigre A. et al. 2009, ApJ, 706, 184

Ménard B., Scranton R., Fukugita M., Richards G. 2010, MNRAS, 405, 1025

Menéndez-Delmestre K., Blain A.W., Alexander D.M., Smail I., Armus L., Chapman S.C., Frayer D.T., Ivison R.J., Teplitz, H.I 2007, ApJ, 655, 65

Menéndez-Delmestre K., Blain A.W., Smail I., Alexander D.M., Chapman S.C., Armus L., Frayer D.T., Ivison R.J., Teplitz, H.I 2009, ApJ, 699, 667

Meng X.-M., Wu H., Gu Q.-S., Wang J., Cao C. 2010, ApJ, 718, 928

Merloni A. 2004, MNRAS, 353, 1035

Miller N.A., Fomalont E.B., Kellermann K.I., Mainieri V., Norman C., Padovani P., Rosati P., Tozzi P. 2008, ApJS, 179, 114

Mineo S., Gilfanov M., Sunyaev R. 2012, MNRAS, 419, 2095

Morrison G.E., Owen F.N., Dickinson M., Ivison R.J., Ibar E. 2010, ApJS, 188, 178

Murray N., Ménard B., Thompson T.A. 2011, ApJ, 735, 66

Myers A.D. et al. 2005, MNRAS, 359, 741

Nandra K., Pounds K. 1994, MNRAS, 268, 405

Narayanan D., Hayward C.C., Cox T.J., Hernquist L., Jonsson P., Younger J.D., Groves B. 2010, MNRAS, 401, 1613

Nardini E., Risaliti G., Salvati M., Sani E., Imanishi M., Marconi A., Maiolino R. 2008, MNRAS, 385, 130

Nenkova M., Sirocky M.M., Ivezic Z., Elitzur M. 2008, ApJ, 685, 147

Noll S., Burgarella D., Giovannoli E., Buat V., Marcillac D., Munoz-Mateos J.C. 2009, A&A, 507, 1793

Oppenheimer B.D., Davé R. 2006, MNRAS, 373, 1265

Peebles P.J.E. 1980, The Large Scale Structure of the Universe (Princeton: Princeton Univ. Press)

Perera T.A et al. 2008, MNRAS, 391, 1227

Pérez-González P.G. et al. 2005, ApJ, 630, 82

Persic M., Rephaeli Y. 2002, A&A, 382, 843

Persic M., Rephaeli Y., Braito V., Cappi M., Della Ceca R., Franceschini A., Gruber D.E 2004, A&A, 419, 849

Persic M., Rephaeli Y. 2007, A&A, 463, 481

Pope A. et al. 2006,, MNRAS, 370, 1185

Pope A. et al. 2008, ApJ, 675, 1171

Press W.H., Teukolsky S.A., Vetterling W.T., Flannery B.P. 1992, Numerical Recipes in C: The Art of Scientific Computing, 2nd edn. Cambridge Univ., Cambridge

Ranalli P., Comastri A., Setti G. 2003, A&A, 399, 39

Roche N.D., Dunlop J., Almaini O. 2003, MNRAS, 346, 803

Rowan-Robinson M. 1992, MNRAS, 258,787

Rowan-Robinson M. et al. 2010, MNRAS, 409, 2

Santini P., Fontana A., Grazian A., Salimbeni S., Fiore1 F., Fontanot F., Boutsia K., Castellano M., Cristiani S., De Santis C., Gallozzi S., Giallongo E., Menci N., Nonino M., Paris D., Pentericci L., Vanzella E. 2009, A&A, 504, 751

Shloerb F.P. 2008, SPIE, 7012E, 26

Scott K.S. et al. 2008, MNRAS, 385, 2225

Scott K.S. et al. 2010, MNRAS, 405, 2260

Scott K.S. et al. 2012, MNRAS, submitted, arXiv:1203.2609

Serra P. et al. 2011, ApJ, 740, 22

Sejeant S. et al. 2010, A&A, 514, 10

Siebenmorgen R., Freudling W., Krugel E., Haas M. 2004, A&A, 421, 129

Siebenmorgen R., Efstathiou A. 2005, in The Spectral Energy Distributions of Gas-Rich Galaxies: Confronting Models with Data, AIP Conference Proceedings Vol. 761, 245

Silva L., Granato G.L., Bressan A., Danese L. 1998, ApJ, 509,103

Silverman J.D. et al. 2010, ApJS, 191, 124

Smail I., Ivison R.J., Blain A.E. 1997, ApJL, 490, L5

Smail I., Chapman S.C., Blain A.W., Ivison R.J. 2004, ApJ, 616, 71

Swinbank A.M. et al. 2010, Nature, 464, 733

Tacconi L.J. et al. 2006, ApJ, 640, 228

Tacconi L.J. et al. 2008, ApJ, 680, 246

Tamura Y. et al. 2010, ApJ, 724, 1270

Tozzi P. et al. 2000, A&A, 451, 457

Valiante E., Lutz D., Sturm E., Genzel R., Tacconi L.J., Lehnert M.D., Baker A.J. 2007, ApJ, 660, 1060

Vieira J.D. et al. 2010, ApJ, 719, 763

Wang Q.D. 2004, ApJ, 612, 159

Weiβ A. et al. 2009, ApJ, 707, 1201

Wilson G.W. et al. 2008, MNRAS, 386, 807

White N.E., Swank J.H., Holt S.S. 1983, ApJ, 270, 711

Williams C.C. et al. 2011, ApJ, 733, 92

Xue Y. Q. et al. 2011, ApJS, 195, 10

Younger J.D. et al. 2007, ApJ, 671, 1531

Younger J.D. et al. 2008, ApJ, 688, 59

Younger J.D., Hopkins P.F. 2011, MNRAS, 410, 2180

Yun M.S., Reddy N.A., Condon J.J. 2001, ApJ, 554, 803

Yun et al. 2012, MNRAS, 420, 957

Zu Y. Weinberg D.H., Davé R., Fardal M., Katz N., Keres D., Oppenheimer B.D. 2011, MNRAS, 412, 1059